Recent progress in graphitic carbon nitride-based materials for antibacterial applications: synthesis, mechanistic insights, and utilization

Zhang *et al. Microstructures* 2024;4:2024017
DOI: 10.20517/microstructures.2023.77

Microstructures

Review

Open Access

Check for updates

Recent progress in graphitic carbon nitride-based materials for antibacterial applications: synthesis, mechanistic insights, and utilization

Xiaoyu Zhang[1], Xinyu Wu[1], Jian Zhang[2], Huiyan Xu[3], Xin Yu[1,4]

[1]Institute for Advanced Interdisciplinary Research, School of Chemistry and Chemical Engineering, University of Jinan, Jinan 250022, Shandong, China.
[2]Division of Systems and Synthetic Biology, Department of Life Sciences, Chalmers University of Technology, Göteborg 41296, Sweden.
[3]Institute for Smart Materials & Engineering, University of Jinan, Jinan 250022, Shandong, China.
[4]Key Laboratory of Optic-Electric Sensing and Analytical Chemistry for Life Science, MOE, Qingdao University of Science and Technology, Qingdao 266042, Shandong, China.

Correspondence to: Prof. Huiyan Xu, Institute for Smart Materials & Engineering, University of Jinan, No. 336, West Road of Nan Xinzhuang, Jinan 250022, Shandong, China. E-mail: ism_xuhy@ujn.edu.cn; Prof. Xin Yu, Institute for Advanced Interdisciplinary Research, School of Chemistry and Chemical Engineering, University of Jinan, No. 336, West Road of Nan Xinzhuang, Jinan 250022, Shandong, China. E-mail: ifc_yux@ujn.edu.cn

How to cite this article: Zhang X, Wu X, Zhang J, Xu H, Yu X. Recent progress in graphitic carbon nitride-based materials for antibacterial applications: synthesis, mechanistic insights, and utilization. *Microstructures* 2024;4:2024017. https://dx.doi.org/10.20517/microstructures.2023.77

Received: 24 Nov 2023 **First Decision:** 22 Dec 2023 **Revised:** 2 Jan 2024 **Accepted:** 17 Jan 2024 **Published:** 2 Apr 2024

Academic Editor: Chunqiang Zhuang **Copy Editor:** Fangling Lan **Production Editor:** Fangling Lan

Abstract

Recent breakthroughs in graphitic carbon nitride ($g\text{-}C_3N_4$)-based materials have catalyzed the development of highly effective antibacterial strategies. This comprehensive review delves into the synthesis, mechanistic insights, and applications of $g\text{-}C_3N_4$ in the realm of antibacterial research. The introduction first highlights the importance of antibacterial materials, emphasizing the urgent need for innovative solutions in the face of bacterial infections and the escalating challenges posed by antibiotic resistance. Continuing, the structural attributes and distinctive characteristics of $g\text{-}C_3N_4$ are examined in detail, elucidating its inherent properties that make it a compelling candidate for antibacterial applications. Subsequently, we meticulously dissect various methods used in the synthesis of $g\text{-}C_3N_4$, encompassing both top-down and bottom-up approaches, offering valuable insights into the production of this promising nanomaterial. Furthermore, it delves deeper into the sterilization mechanisms of $g\text{-}C_3N_4$-based nanomaterials, encompassing a spectrum of strategies, including physical structure sterilization, photocatalytic antibacterial effects, enzymatic antibacterial processes, and the synergetic benefits that emerge

from the fusion of these mechanisms. Then, it comprehensively examines the practical applications of g-C_3N_4-based nanomaterials in antibacterial endeavors, encompassing their pivotal roles in water purification, air purification, treatment of bacterial infections, and the development of antibacterial layers in diverse settings. In conclusion, we encapsulate the crux of our findings and provide a forward-looking perspective on the potential challenges and opportunities in the arena of g-C_3N_4-based materials for antibacterial applications. This review aspires to galvanize further exploration and innovation in the design of high-performance g-C_3N_4-based materials, thereby contributing to the progression of antibacterial solutions.

Keywords: Graphitic carbon nitride, antibacterial mechanism, photocatalysis, nanozyme, therapy

INTRODUCTION

Bacterial infections have consistently presented a significant global public health challenge, resulting in millions of annual fatalities due to diseases induced by bacterial pathogens[1]. The discovery and utilization of antibiotics since the 1940s have undeniably benefited humanity[2]. However, the escalating reliance on antibiotics has led to a surge in antibiotic-resistant bacteria[3]. If the overuse of antibiotics is not curtailed, bacterial infections could potentially pose a more severe global threat than cancer[4]. Consequently, there is an urgent need for research into novel antibacterial methods[5]. The utilization of nanomaterials in crafting innovative antibacterial agents has emerged as a pivotal approach to combat drug-resistant bacterial infections, with engineered nanomaterials standing out as crucial candidates for the next generation of antibacterial agents[6]. Nanomaterials designed for antibacterial purposes have garnered widespread attention, not just owing to their distinctive physicochemical properties but also due to their easily controllable morphology, characterized by high surface area and porous structures conducive to antibacterial features[7].

As a metal-free two-dimensional (2D) conjugated polymer, graphitic carbon nitride (g-C_3N_4), primarily composed of C and nitrogen (N) atoms, has attracted widespread attention due to its optical properties[8,9]. It has captured attention for its facile synthesis and functionalization, high physicochemical stability, stabilized electron field emission, wide-band optical transparency, controllable band gap and position, and low toxicity[10]. Compared to 2D materials such as MoS_2 and Sn_3O_4, the reactive sites of 2D g-C_3N_4 undergo substantial enhancement owing to the interplay of the quantum confinement effect, multiple scattering effects, and directed charge transfer[11]. This augmentation results in a significant improvement in both the light capture and redox capacities of the material. Moreover, these distinctive properties markedly boost the interaction between g-C_3N_4 and reactants, potentially paving the way for novel reaction pathways and thereby endowing 2D g-C_3N_4 with promising applications[12].

In the realm of photocatalysis, g-C_3N_4-based materials have gained substantial recognition[13,14]. Huang *et al.* pioneered the application of g-C_3N_4 in photocatalytic water splitting and subsequently extended its photocatalytic prowess to the exploration of antibacterial properties[15]. Thurston *et al.* have documented the efficacy of g-C_3N_4 in eradicating *Escherichia coli (E. coli)* and *Staphylococcus aureus* (*S. aureus*) under visible light conditions[16]. The introduction of Ag nanoparticles (NPs) has been demonstrated to significantly enhance the antibacterial properties of g-C_3N_4. In the presence of visible light, Ag-doped g-C_3N_4 proves effective in deactivating *E. coli*, *S. aureus*, and *Pseudomonas aeruginosa* (*P. aeruginosa*)[17]. Sun *et al.* devised a graphene/g-C_3N_4 composite, achieving a remarkable 97.9% reduction in *E. coli* viability after 120 min of visible light exposure[18]. Aquino de Carvalho *et al.* recently revealed that moderate carbon doping enhances the antibacterial activity of g-C_3N_4[19]. Leveraging unique physicochemical attributes and photo-oxidizing and photocatalytic activity of ZnO NPs[20,21], the ZnO/g-C_3N_4 composite exhibits outstanding antibacterial efficacy against both gram-negative and gram-positive bacteria[22]. Recent investigations indicate that metal-

doped ZnO/g-C_3N_4 composites further amplify the antibacterial capabilities of ZnO/g-C_3N_4[23,24]. Furthermore, quantum dots (QDs) of g-C_3N_4 were synthesized by Dai *et al*., revealing enzymatic catalytic activity capable of catalyzing H_2O_2 to generate reactive oxygen species (ROS) with potent antibacterial effects[25]. Wang *et al*. introduced doping into g-C_3N_4, creating a catalyst with a synergistic effect of photocatalysis and nanozymes for bacteria-killing, which exhibited robust antibacterial effects, promoting the proliferation and migration of epidermal cells and facilitating the rapid healing of infected wounds[26].

This comprehensive review delves into the synthesis, antibacterial mechanisms, and practical applications of g-C_3N_4-based nanomaterials. Firstly, the structural characteristics of g-C_3N_4 are introduced, emphasizing its inherent features that make it a strong candidate material for antibacterial applications. Subsequently, the synthesis methods of g-C_3N_4-based nanomaterials are detailed, including both top-down and bottom-up approaches, providing valuable insights for the production of this promising nanomaterial. Following that, there is a further in-depth exploration of the sterilization mechanisms of g-C_3N_4-based nanomaterials, encompassing physical structure sterilization, photocatalytic antibacterial effects, enzyme antibacterial processes, and the synergistic effects generated by these mechanisms. A comprehensive examination is then conducted regarding the practical applications of g-C_3N_4-based nanomaterials in antibacterial work, including water purification, air purification, treatment of bacterial infections, and the development of antibacterial coatings. Finally, prospects are provided for the potential challenges and opportunities in the field of antibacterial applications of g-C_3N_4-based nanomaterials.

STRUCTURE OF g-C_3N_4

g-C_3N_4, a non-metallic polymer, shares a structural resemblance with graphene, featuring sp^2 hybridized C and N atoms forming an aromatic C-N hexatomic ring[27]. This compound boasts a highly dispersed π-electron conjugation system within its 2D network structure[28]. The architecture of g-C_3N_4 comprises a stacked 2D layered structure with an interlayer spacing of 0.326 nanometers, stabilized by weak van der Waals interactions between the layers[29]. Owing to its rigid C-N heterocyclic network structure, highly conjugated system, and notable degree of condensation, g-C_3N_4 displays outstanding thermal and chemical stability[30,31]. Its remarkable heat resistance extends up to 600 degrees Celsius, surpassing that of all other organic materials. Furthermore, it remains insoluble in water, most acids, bases, and various organic solvents.

Structurally, g-C_3N_4 exists in two forms of isomers: one is constituted by s-triazine (Figure 1A, C_3N_3), and the other employs tri-s-triazine (Figure 1B, C_6N_7) as building blocks. Different repeating units connect through tertiary amino groups, giving rise to a planar structure. The size of periodic vacancies in the lattice and the distinct electronic environment of N atoms contribute to varying energy stabilities. According to first-principles density functional theory (DFT) calculations, the more stable tri-s-triazine is typically regarded as the primary structural unit of g-C_3N_4[32].

Based on theoretical computations, g-C_3N_4 manifests the prototypical attributes of an indirect bandgap semiconductor. Positioned on opposing sides of the Fermi level, the conduction and valence bands (VB) exhibit distinct minima and maxima, with the conduction band (CB) bottoming out at -1.1 eV and the VB peaking at +1.6 eV. Notably, these bands do not overlap in k-space, defining a bandgap width of approximately 2.7 eV [Figure 1C][33]. In a low-coordination setting, the VB is primarily governed by the N atomic orbitals of aromatic CN heterocycles, while the CB results from the combined C and N atomic orbitals of CN heterocycles [Figure 1D]. The sp2 hybridized C and N atoms establish highly conjugated π bonds, creating a polymer system with pronounced electron delocalization, evidenced by a pair of lone electrons on the pz orbitals [Figure 1E and F]. The work function of g-C_3N_4 approximates 4.50 eV,

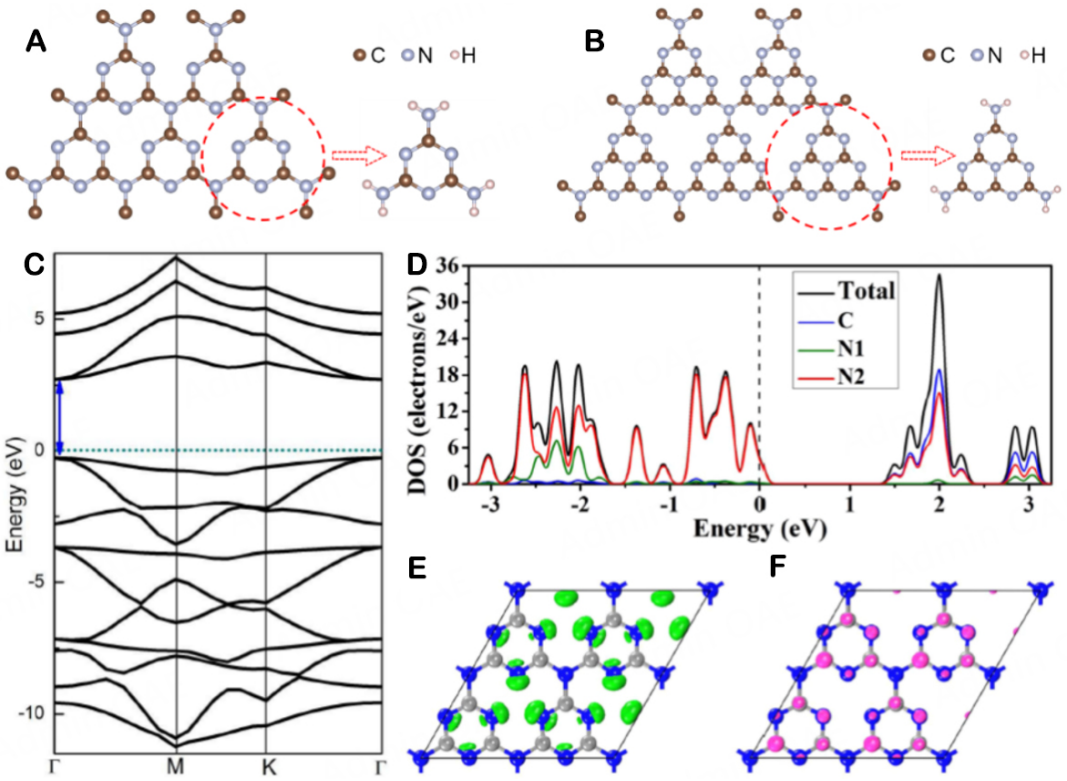

Figure 1. (A) Triazine and (B) tri-s-triazine structures of g-C_3N_4. (C) Band structures of monolayer g-C_3N_4. (Reproduced with permission[33]. Copyright 2016, Royal Society of Chemistry). (D) Density of states (DOS), (E) highest occupied molecular orbital (HOMO), and (F) lowest unoccupied molecular orbital (LUMO) of monolayer g-C_3N_4. (Reproduced with permission[34]. Copyright 2019, Wiley-VCH).

signifying that a minimum of 4.50 eV energy is requisite for electron migration from the interior to the surface[34]. In the ultraviolet-visible (UV-vis) absorption spectrum, the absorption edge of g-C_3N_4 occurs around 420 nm, aligning with its light yellow hue[35].

The physicochemical attributes of g-C_3N_4 intricately correlate with its structural constitution. Given the tuneability of its structure, all devised techniques for material modification find applicability with g-C_3N_4. For instance, altering morphology, enhancing specific surface area, and refining optical properties are achieved by various means[36-38]. Introducing dopant atoms, creating surface defects, and refining electronic structures represent avenues for improvement[39]. Building composite systems with other semiconductors or enhancing overall crystalline structures aims to boost charge carrier separation and migration capabilities[40]. Furthermore, employing the distinctive molecular engineering strategy of organic semiconductors, integrating organic groups into N-doped graphene-like carbon facilitates functional modification[41,42]. Consequently, with its outstanding stability and adaptable structure-performance interplay, N-doped graphene-like carbon furnishes a steadfast, dependable, and versatile material platform across fields such as condensed matter physics, synthetic chemistry, nanomaterials science, and various applications, holding considerable promise for research and practical applications.

SYNTHESIS METHOD OF g-C_3N_4

The synthesis of g-C_3N_4 involves utilizing C- and N-rich small molecules (e.g., melamine, thiourea, urea, cyanuramide, and dicyandiamide) as raw materials, with the synthesis process employing straightforward

heating. This cost-effective and easily operable method has been highlighted[37,43]. Taking cyanuramide as an illustrative case[44], the transformation cascade begins at 150 °C, progressing from cyanuramide to dicyandiamide and further evolving into melamine at 240 °C. As the temperature climbs to 390 °C, the initial formation of C_6N_7 units takes place, culminating at around 520 °C with the formation of g-C_3N_4 through additional deamination-condensation reactions. However, g-C_3N_4 obtained via conventional thermal condensation methods typically exhibits reduced surface area and suboptimal photocatalytic performance, often described as bulk or block-like g-C_3N_4. Highly active g-C_3N_4 typically showcases small particle size, a substantial surface area, or distinctive micro-nano structures. These attributes expose numerous catalytic active sites, promoting efficient electron transfer and heightened light absorption capabilities. Consequently, researchers have explored innovative methods in the synthesis of micro-nanostructured g-C_3N_4, including salt melting, microwave-assisted synthesis, stripping, and template techniques.

Salt melting method

In elevated temperature environments, the creation of molten salt melts augments the mobility of reaction components in the liquid phase, resulting in a significant increase in diffusion rates. Concurrently, the crystalline framework of the molten salt itself can function as a synthesis template[45,46]. Miller *et al.*, employing a LiBr/KBr low eutectic mixture and melamine, achieved the successful production of single-crystal g-C_3N_4 through combined calcination[47]. Ou *et al.* utilized a composite molten salt composed of lithium chloride and potassium chloride (KCl), along with melamine, to synthesize highly crystalline g-C_3N_4 featuring heptazine ring structural units[48]. In the molten salt method of g-C_3N_4 synthesis, beyond the molten salt and raw materials, additional monomers can be introduced to enhance or adjust the structure and properties of g-C_3N_4. Zhang *et al.*, by individually calcining NaCl/KCl and nucleic acid bases with N-rich organic compounds at 550 °C, successfully obtained g-C_3N_4 with internal heterostructures[49]. To explore the impact of different molten salts on the structure and properties of g-C_3N_4, Guo *et al.* employed LiCl/KCl, LiCl/NaCl, and NaCl/KCl as low-melting-point salts. The results indicated that g-C_3N_4 synthesized with LiCl/NaCl as the molten salt exhibited the least defects and the most extensive π-conjugated structure[50]. Moreover, besides serving as a flowable medium at high temperatures, molten salts can act as a template in the thermal condensation process, facilitating the direct synthesis of 2D g-C_3N_4 nanosheets (NSs) based on their crystalline structure. Guo *et al.* successfully synthesized highly ordered planar g-C_3N_4 NSs using pure NaCl as the molten salt. In the synthesis process [Figure 2A], NaCl played three pivotal roles: firstly, its high surface energy facilitated the adsorption and activation of melamine on its crystal face; secondly, NaCl served as a 2D self-assembly template for g-C_3N_4 NSs; finally, Na ions could enter the structure of g-C_3N_4 NSs as doping elements, acting as basic sites[51].

Liang *et al.* elucidated the molecular-level evolution mechanism of poly(triazine imide) (PTI) crystals through the thermal polymerization in molten salts. Leveraging ionothermal methods to enhance mass transfer and catalyze polymerization, a crystallinity-enhanced conjugation product, namely PTI, was successfully obtained in KCl-LiCl molten salts[52]. Figure 2B illustrates a detailed molecular-level evolution mechanism governing the thermal polymerization of PTI crystals within molten salts. During the heating stage, employing melon as the precursor initiates the formation of eutectics above the eutectic point with KCl and LiCl salts. The heptazine-based melon undergoes depolymerization into triazine structural units within the low-melting-point molten salt. Upon elevating the temperature to 550 °C, Li^+ and Cl^- ions intercalate into triazine units, resulting in the formation of PTI molecular units that exhibit solubility in molten salts. In the subsequent cooling stage, the liquid becomes supersaturated with PTI monomers and salts below the eutectic temperature, leading to the precipitation of KCl cubes as the primary phase. These KCl cubes expose {100} flat facets, serving as templates for guiding the directional stacking of PTI molecular units on the {0001} planes in a layer-by-layer manner, ultimately forming a pristine prism without

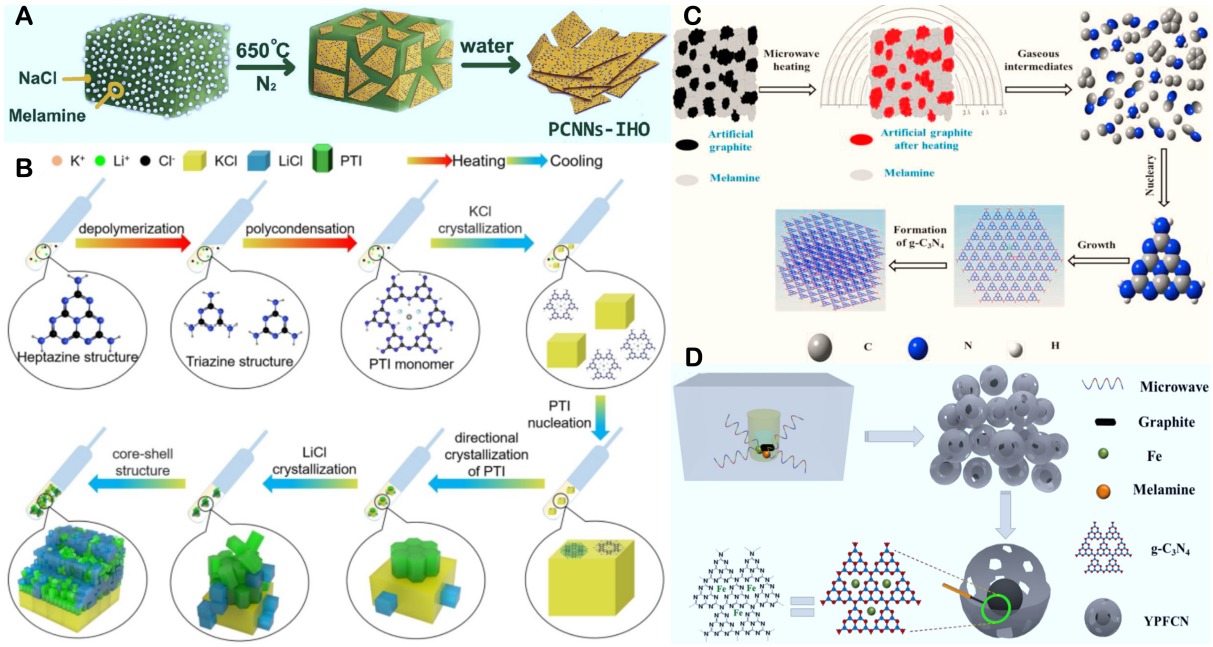

Figure 2. (A) Illustration for the synthesis process of PCNNs-IHO by on-surface polymerization. (Reproduced with permission[51]. Copyright 2021, Wiley-VCH). (B) Schematic diagram of the molecular conjugation and directional crystallization processes of PTI polymer crystals in molten salts. (Reproduced with permission[52]. Copyright 2023, Wiley-VCH). (C) Schematic illustration of the formation of MCN via microwave heating. (Reproduced with permission[14]. Copyright 2016, Elsevier). (D) Schematic illustration of the proposed formation mechanism of YPFCN. (Reproduced with permission[31]. Copyright 2018, Elsevier).

truncation. A parallel heterogeneous nucleation process is observed for LiCl salts on the {001} surfaces of KCl cubes, creating an interpenetrated microstructure alongside PTI crystals. The organized directional condensation of triazine layers results in vertically aligned PTI crystals on KCl templates, avoiding the introduction of observable structural defects. As PTI and LiCl crystals grow in size, the KCl templates become isolated from the molten liquid. In the absence of KCl cubes as directional crystallization templates, newly nucleated PTI crystals gradually deviate from the orientation of the KCl matrix, giving rise to a texture-like microstructure[52]. In addition to salt acting as a low-melting-point medium, sulfur was employed as a reaction solvent during the heating process to prepare highly active g-C_3N_4 films[53].

Microwave method

In contrast to conventional heating methods such as thermal radiation or conduction, microwave heating induces rapid oscillation of polar molecules within an object. This phenomenon results in frictional losses between neighboring molecules responding to the fluctuating electromagnetic field. The consequent conversion of microwave energy into heat leads to a temperature increase in the object. This unique heating approach is a collective outcome of the interactions among all polar molecules within the object, providing advantages such as heightened reaction rates, selectivity, and energy efficiency. Widely recognized as a pivotal strategy for achieving environmentally friendly processes[54,55], microwave heating has garnered substantial attention.

Yuan *et al.* employed melamine as a precursor and copper oxide powder as a microwave-absorbing heat source to successfully synthesize highly crystalline g-C_3N_4 through microwave irradiation[56]. Furthermore, by substituting raw materials with dicyandiamide, thiourea, and others, g-C_3N_4 synthesis was achieved using the same microwave process. The efficacy of microwave heating technology is intricately linked to microwave power and the type of microwave absorber. Yu *et al.* utilized graphite powder as a microwave

absorber and melamine as the raw material, successfully synthesizing highly crystalline g-C_3N_4 under conditions of 4 kW microwave power and high vacuum [Figure 2C][14]. They observed that increasing the power facilitated the preparation of g-C_3N_4 NSs[14]. Additionally, they proposed a distinctive thermal condensation process for g-C_3N_4 synthesis. Under intense microwave irradiation and rapid heating in high vacuum, graphite powder interacted strongly with microwaves. This interaction led to vigorous plasma ignition, generating highly reactive and non-steady-state carbon atoms or clusters from the graphite powder. This process promoted the decomposition and combination of melamine, realizing the rapid synthesis of g-C_3N_4. Moreover, researchers explored the synthesis of 2D g-C_3N_4 structures with fewer layers or single layers using carbon fibers as a more responsive microwave absorber[57]. The study revealed that, with melamine as the precursor and carbon fibers as the microwave absorber, a 2D g-C_3N_4 NS with a surface area of 239 m^2/g and a thickness of approximately 1.6 nm was obtained under conditions of 5 kW microwave power and high vacuum. By extending the reaction time, a pyramid-shaped morphology of g-C_3N_4 was achieved. Furthermore, by incorporating iron powder as the second microwave absorber and a doping element, researchers successfully synthesized a porous core-shell structured iron-doped g-C_3N_4 under microwave conditions [Figure 2D][31].

Stripping method

The technique of delamination typically initiates with the synthesis of bulk g-C_3N_4, followed by approaches such as ultrasonication-assisted liquid-phase delamination and thermal etching delamination, strategically employed to overcome van der Waals forces between layers. This process yields 2D structures in the form of g-C_3N_4 NSs. In a study by Yang *et al.*, a comparative exploration of ultrasonic delamination effects in various solvents revealed that isopropanol, characterized by appropriate surface energy and a low boiling point, yielded optimal results[58]. Following 10 h of ultrasonic treatment, high surface area and ultrathin g-C_3N_4 NSs were attained. Moreover, a molten salt method was utilized to synthesize high-crystallinity g-C_3N_4, serving as a precursor for ultrasonication-assisted liquid-phase delamination. This process resulted in high-crystallinity g-C_3N_4 NSs with a surface area of approximately 203 m^2/g and a thickness of approximately 3.6 nm[48]. To mitigate potential ecological risks associated with organic solvents, Zhang *et al.* opted for water as a solvent, achieving ultrathin g-C_3N_4 NSs with a diameter of around 100 nm and a thickness of 2.5 nm through ultrasonic delamination [Figure 3A][59]. Acknowledging the prolonged nature of ultrasonic delamination, Niu *et al.* subjected bulk g-C_3N_4 to oxidative etching in an air atmosphere[60]. Over time, multilayered blocks gradually transitioned into fewer or single-layered NS structures, as depicted in Figure 3B. Following 2 h of etching at 500 °C, ultra-thin 2D g-C_3N_4 was successfully obtained. In a collaborative effort, Han *et al.*, combining freeze-drying and solvent-assisted thermal delamination techniques, effectively crafted porous g-C_3N_4 NSs[61]. This distinctive porous architecture not only augmented the specific surface area and widened diffusion pathways for substances but also facilitated the separation of photogenerated electron-hole pairs.

Template method

To engineer micro/nanoparticles with precise size control and prevent agglomeration, template methods leverage the spatial confinement effect for the controlled synthesis of micro/nanomaterials, influencing aspects such as size, morphology, and structure[62,63]. Template methods can be categorized into hard template methods and soft template methods based on the template morphology[64]. Liu *et al.* employed a salt-template-assisted incorporation strategy to prepare highly crystalline g-C_3N_4 with potassium and sulfur dual active sites (K/S@CN_{-x}) [Figure 3C][65]. Initially, KCl and thioacetamide (TAA) were mixed and ground with melamine to form a mixture containing a small amount of anhydrous ethanol. Subsequently, the formed mixture was thermally polymerized at 600 °C under atmospheric conditions to yield a crude product. Finally, through washing and drying of the aforementioned crude product, a highly crystalline K/S@CN_{-x} was obtained[65]. Hard template methods provide a means to regulate the size, morphology,

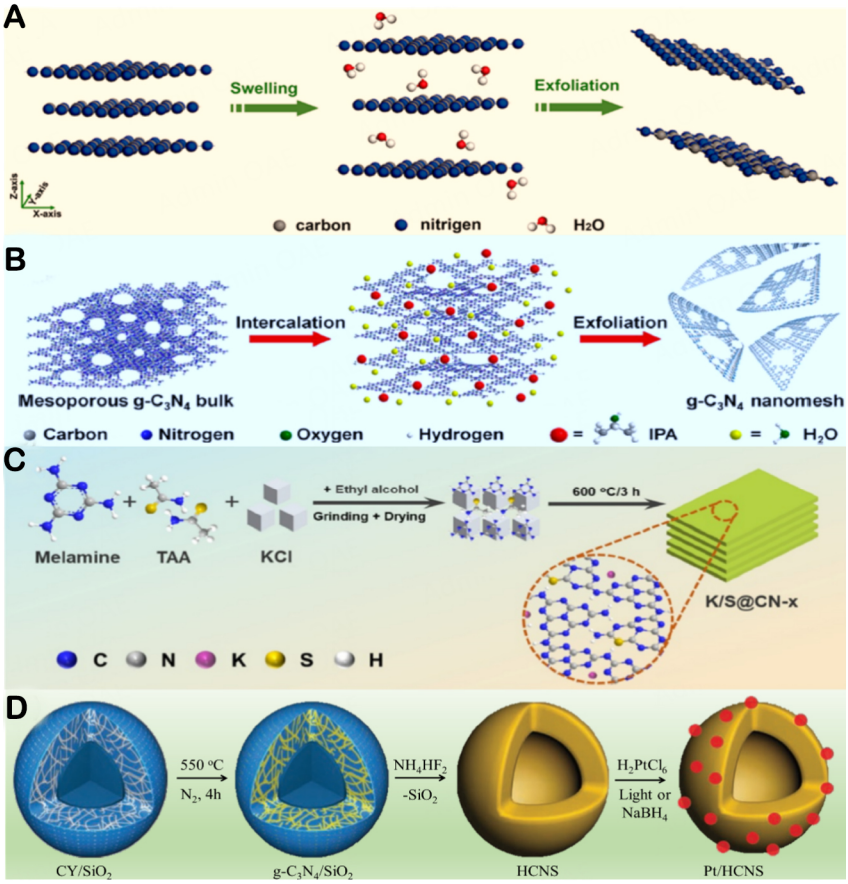

Figure 3. (A) Schematic illustration of liquid-exfoliation process from bulk g-C_3N_4 to ultrathin nanosheets. (Reproduced with permission[59]. Copyright 2013, American Chemical Society). (B) Schematic illustration of solvothermal exfoliation process from mesoporous g-C_3N_4 bulk to nanomesh. (Reproduced with permission[61]. Copyright 2016, American Chemical Society). (C) Schematic illustration for the preparation of K/S@CN_{-x} photocatalysts. (Reproduced with permission[65]. Copyright 2023, American Chemical Society). (D) An illustration of the HCNS and metal/HCNS composite syntheses. (Reproduced with permission[37]. Copyright 2012, Springer Nature).

structure, and specific surface area of g-C_3N_4 owing to the adjustable dimensions and shapes of the template agent. Sun *et al.* employed SiO_2 nanospheres as a template, combined with dicyandiamide, and subjected the mixture to uniform calcination[37]. Through subsequent etching of SiO_2 with a specific concentration of ammonium hydrogen fluoride (NH_4HF_2), they achieved the fabrication of hollow-structured g-C_3N_4 [Figure 3D]. Zheng *et al.* further optimized the crystal and chemical structure of g-C_3N_4 by applying additional heat treatment, maintaining the integrity of the hollow sphere structure[66]. Besides SiO_2 NPs, commonly used hard template agents encompass mesoporous SiO_2 and anodized aluminum oxide (AAO)[67,68]. Nonetheless, the removal of hard templates often involves strong acids or bases, posing potential environmental and health risks, and the processing time is relatively prolonged.

Soft template methods for g-C_3N_4 synthesis typically employ amphiphilic surfactant molecules and specific block copolymers as templates[69,70]. These molecules assemble on the soft template surface through non-covalent bonds, followed by thermal treatment to eliminate the soft template and yield the desired nanostructured material. However, g-C_3N_4 synthesized using soft template methods often retains residual carbon, introducing impurities into the phase.

STERILIZATION MECHANISM OF g-C_3N_4-BASED NANOMATERIALS

Physical bacteria-killing

Characterized by their unique NS-like structure, 2D materials inherently possess antibacterial properties without the need for external stimuli. Their knife-like sharp edges physically sever bacteria, disrupting bacterial cell walls and membranes, causing cellular dysfunction, and resulting in the release of cytoplasmic components[71]. Validation of these effects can be achieved through scanning electron microscopy images or by assessing the liberation of bacterial intracellular components such as RNA, ATP, and proteins[72,73]. The underlying mechanism is schematically illustrated in Figure 4A[74]. The antibacterial efficacy is influenced by several factors, including layer count, length, dispersion, and, notably, the orientation of 2D nanomaterials[75]. Orientation dictates the insertion angle of NSs and the density of sharp edges, with vertically oriented antibacterial activity generally surpassing that of randomly oriented and horizontally oriented counterparts[76]. Bacterial type, culture conditions (such as shaking speed or external magnetic fields), and synergies with other mechanisms (such as oxidative damage) can also influence the antibacterial activity of 2D nanomaterials[77,78].

As a facilely prepared and adaptable 2D nanomaterial, g-C_3N_4 has demonstrated specific antibacterial activity through physical/mechanical disruptive mechanisms. In a recent investigation, Cui *et al.* unveiled N plasma-treated g-C_3N_4 NSs (N-g-C_3N_4) exhibiting broad-spectrum and highly efficient antibacterial activity. The compression of N-g-C_3N_4-treated material induces discernible distortion in bacterial cells, as illustrated in Figure 4B and C[79]. Additionally, the intracellular release of biological macromolecules into the extracellular milieu, as depicted in Figure 4D, signifies that the N-g-C_3N_4 interaction with bacterial cell membranes results in irreversible cellular apoptosis through membrane rupture. Figure 4E illustrates the ability of N-g-C_3N_4 to integrate into the bacterial cell membrane and engage with phospholipid molecules, akin to previously mentioned 2D antibacterial materials, thereby instigating the rupture of cell membranes[79].

Photocatalytic bacteria-killing

Photocatalytic antibacterial technology leverages semiconductor materials, rooted in the absorption of photons by semiconductor catalysts under illumination, culminating in the generation of electron-hole pairs[80]. These pairs subsequently engage with surface substances, such as H_2O and O_2, yielding highly ROS renowned for their exceptional antibacterial efficacy[81]. The efficacy of g-C_3N_4 in photocatalytic antibacterial applications hinges predominantly on the separation and migration dynamics of photoinduced charge carriers[82]. However, unaltered g-C_3N_4 manifests crystal structure defects and a block-like configuration, leading to a scarcity of defect sites for the swift recombination of photoinduced electrons and holes, thereby causing a marked decline in photocatalytic activity[83].

The distinctive layered architecture of g-C_3N_4 facilitates the efficient migration of charge carriers across interfaces, within planes, and between layers. To enhance the charge characteristics of g-C_3N_4, extensive investigations, such as the utilization of Ag NPs to modify g-C_3N_4 and craft Ag/g-C_3N_4 heterostructures, have been undertaken[84]. This modification enhances visible light absorption through the surface plasmon resonance effect, mitigating the recombination of electron-hole pairs and achieving remarkable bactericidal effects against *E. coli*, surpassing the performance of pure g-C_3N_4 NSs. In contrast to pure g-C_3N_4 NSs, Ag/g-C_3N_4 nanohybrids exhibit heightened antibacterial efficiency under visible light, presenting a novel avenue for g-C_3N_4 photocatalytic antibacterial strategies.

In addition to Ag/g-C_3N_4, other effective modification strategies encompass Graphene/g-C_3N_4 and g-C_3N_4/TiO_2 (CT)[85,86]. TiO_2, renowned for its activity and stability in the ultraviolet (UV) region, when combined

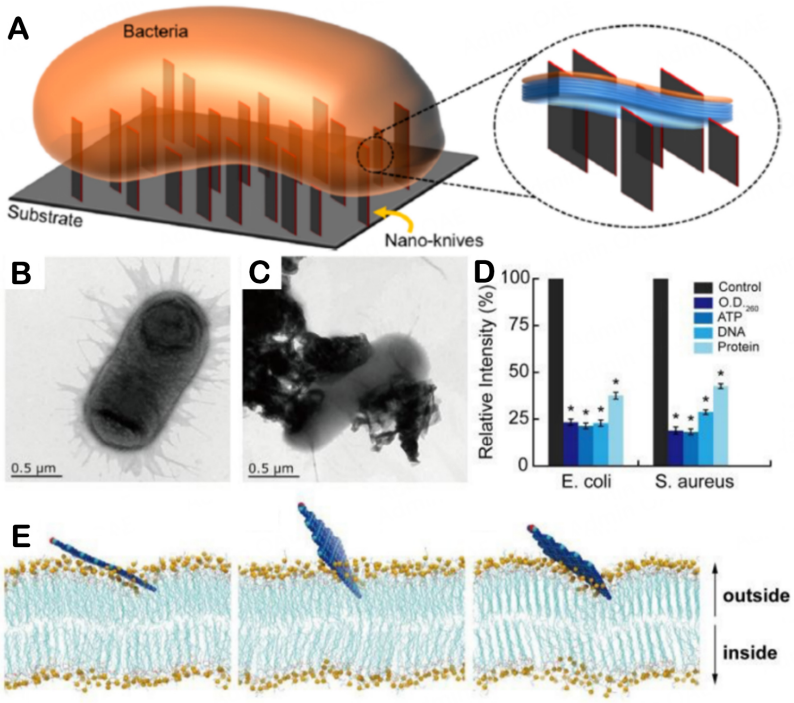

Figure 4. (A) Schematic illustration of the physical bacteria-killing effect caused by 2D nanomaterials on bacteria. (Reproduced with permission from[74]. Copyright 2018, American Chemical Society). (B and C) Transmission electron microscope (TEM) images of *E. coli* and *E. coli* treated with N-g-C_3N_4. (D) Relative intensity of total O.D.260 and relative amount of intracellular ATP, DNA, and total soluble proteins of *E. coli* and *S. aureus* after being treated with N-g-C_3N_4, the bacterial cells without N-g-C_3N_4 as a control group; (E) Final snapshots of g-C_3N_4 NSs interacting with the lipids of the bacterial membrane in three independent trajectories. The upper lipids of the membrane represented the outer layer of the bacterial plasma membrane. (Reproduced with permission from[79]. Copyright 2019, Royal Society of Chemistry).

with g-C_3N_4, yields composite photocatalysts of high efficiency. CT heterostructures, synthesized through a hydrothermal annealing method, showcase superior bactericidal activity under visible light, achieving complete inactivation of *E. coli* within a mere 180 min. This is ascribed to the judicious band alignment within CT heterostructure, fostering more effective separation of photoinduced carriers, thereby enhancing interface charge transfer efficiency.

Concerning interface modification, the introduction of external impurities emerges as a straightforward and effective approach to enhance the separation and migration of charge carriers[87,88]. Internal modification methods span heterogeneous non-metal doping, non-metal self-doping, non-metal/metal co-doping, molecular/functional group modification, metal doping, defect design, and plasma design[89,90]. External modification strategies include carbon dot/carbon QD coupling, metal QD coupling, plasma coupling, single-atom modification, constructing heterojunctions, and homo-heterojunctions[91,92]. These strategies, through adjustments in interface charge transfer, effectively elevate the performance of photocatalytic antibacterial agents[93].

Furthermore, the morphological diversity of semiconductor materials, typically influenced by the manipulation of specific surface area and crystal face exposure, also applies to g-C_3N_4. For instance, researchers have successfully prepared atomic monolayer g-C_3N_4 with a mere 0.5 nm thickness, demonstrating significantly enhanced photocatalytic activity against *E. coli* under visible light irradiation for 4 h, outperforming block-like g-C_3N_4 and thermally etched g-C_3N_4 NSs[94]. Che *et al.* designed an innovative

and more efficient S-type heterojunction between 2D phosphorus-doped g-C_3N_4 (P-g-C_3N_4) and BiOBr using hydrothermal polymerization. This design aimed to suppress charge recombination and expand the light absorption range[95]. The P-g-C_3N_4/BiOBr hybrids demonstrated significantly enhanced photocatalytic disinfection performance compared to g-C_3N_4/BiOBr under visible wavelengths, suggesting that phosphorus doping, which adjusts the band structure, plays a crucial role in the S-type heterojunction system. The sterilization rate for multidrug-resistant *Acinetobacter baumannii 28* (*AB 28*) reached 99.9999% within 80 min, and for *S. aureus*, it was 99.9%[95].

Xia *et al.* explored the development of 0D/2D S-type heterojunctions on polymeric carbon nitride (pCN) for visible-light-driven photocatalytic inactivation of bacteria[96]. The S-type heterojunction system, serving as an innovative photocatalytic platform, exhibits substantial potential in facilitating the separation and transfer of photogenerated charge carriers, leading to robust photo-oxidation-reduction capabilities [Figure 5A]. Employing an *in situ* wet chemistry approach followed by heat treatment, the researchers engineered a 0D/2D S-type heterostructure by incorporating CeO_2 QDs into the pCN framework (pCN/CeO_2). Under visible light exposure ($\lambda \geq 420$ nm), the pCN/CeO_2 demonstrated an impressive photocatalytic sterilization efficiency of 88.1% against *S. aureus*, surpassing the performance of pure CeO_2 (32.2%) and pCN (10.7%) by factors of 2.7 and 8.2, respectively [Figure 5B][96].

Additionally, He *et al.* presented a specialized dual-functional 2D/2D g-C_3N_4/BiO_{2-x} NS heterojunction prepared through a self-assembly method [Figure 5C][97]. This resulting heterojunction displayed effective photocatalytic disinfection performance against *E. coli* under visible light irradiation, attributed to the advantageous migration of photogenerated carriers at the Z-scheme interface. Near-infrared (NIR) light-induced photocatalytic enhancement was ascribed to the synergistic effects of photothermal and "hot electron" processes, facilitating efficient charge transfer [Figure 5D and E]. During the sterilization process, cell membranes were compromised, evidenced by the generation of lipid peroxidation and disruption of energy metabolism. Subsequently, enzyme impairment and the release of intracellular components indicated the irreversible death of *E. coli* K-12[97].

Nanozyme bacteria-killing

The intrinsic peroxidase (POD)-like activity of g-C_3N_4 is modest; nevertheless, owing to its secure and cost-effective attributes, it emerges as an outstanding host for materials with robust enzymatic catalytic capabilities[98]. Wang *et al.* adeptly combined colloidal Au NPs with ultrathin g-C_3N_4, yielding a novel composite material that showcases exceptional POD-like activity and efficient catalytic performance[99]. This synergistic structure transforms H_2O_2 into hydroxyl radicals, demonstrating striking antibacterial effectiveness against both Gram-negative and Gram-positive bacteria. Additionally, it exhibits favorable outcomes in breaking down existing bacterial biofilms and preventing the formation of new ones.

Furthermore, a deeper understanding of the active center structure of natural enzymes serves as a blueprint for enhancing the selectivity and catalytic activity of g-C_3N_4-based nanomaterials. Defect engineering has become a prevalent strategy for adjusting the electronic structure and refining the performance of nanozymes[100]. Numerous metal-based defective nanomaterials, such as MoS_2, reportedly manifest POD-like activity. Abundant defects induce cracking in the crystal structure on the substrate surface, amplifying active sites and facilitating electron transfer between the substrate and neighboring electrons[101]. Simultaneously, carbon-based nanozymes have attracted widespread attention due to their renewable nature, biocompatibility, and cost-effectiveness[102]. Zero-dimensional point defects arising from N vacancies in g-C_3N_4 can modify the local electron distribution and extend π-electron delocalization, exposing plentiful coordinatively unsaturated sites. These sites not only proficiently adsorb substrates but also activate H_2O_2, generating copious ROS to enhance antibacterial activity.

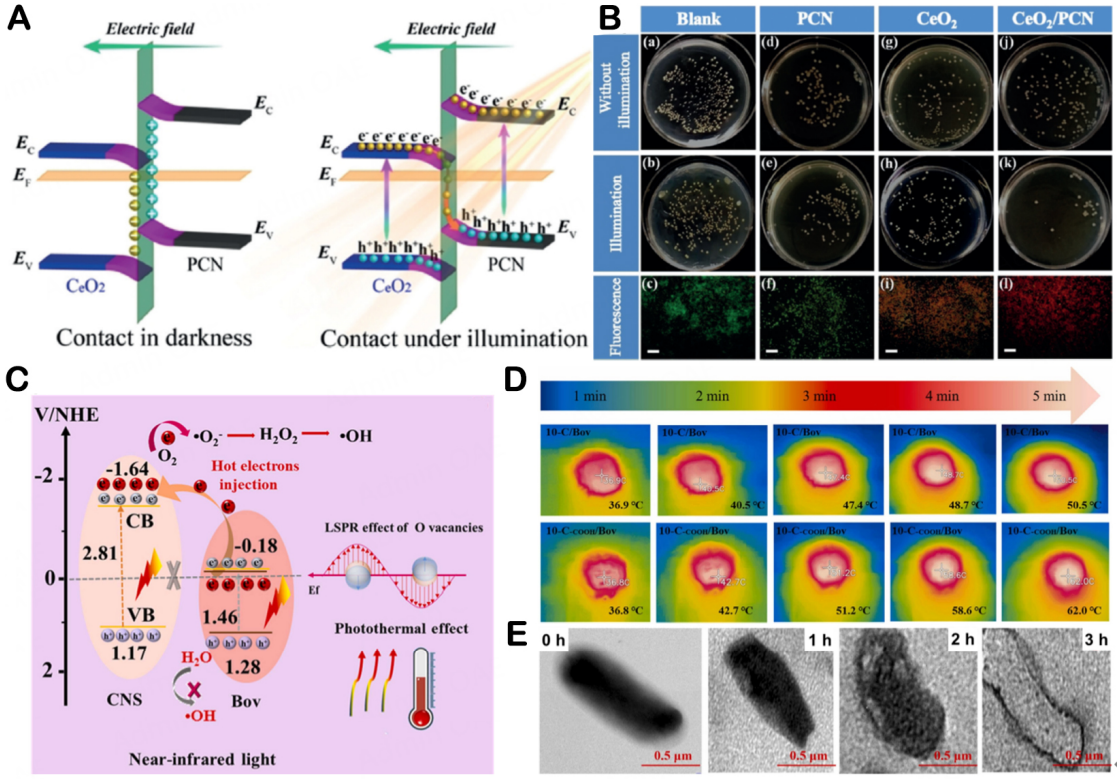

Figure 5. (A) The S-scheme transfer mechanism of photogenerated electrons in darkness and under the illumination. (B) The antibacterial effects without illumination, under illumination, and corresponding fluorescent dye mapping images over the blank experiment, pCN, CeO_2, and pCN/CeO_2 composites, respectively. The green and red areas represent the living and dead bacteria, respectively. (Reproduced with permission[96]. Copyright 2020, Wiley-VCH). (C) Mechanism of photocatalytic disinfection over 10-CNS/Bov. (D) The infrared photothermal images of 10-C/Bov and 10-C-COOH/Bov. (E) The individual and overall morphology change of the *E. coli* K-12 before and after disinfection for 1, 2, and 3 h over10-CNS/Bov under NIR light irradiation. (Reproduced with permission[97]. Copyright 2022, Elsevier).

Dai *et al.* employed a straightforward ultrasonic fragmentation method to prepare N-deficient g-C_3N_4 QD (CNQD) nanozymes for broad-spectrum antibacterial applications [Figure 6A][25]. Structural models detailing the absorption of H_2O_2 on g-C_3N_4 and CNQDs were established through DFT calculations. The computed electronic localization function (ELF) results indicated H_2O_2 adsorption energies of -2.265 and -7.432 eV for CN and CNQDs, respectively. These outcomes underscored that CNQDs featuring N vacancies displayed remarkable POD-like catalytic efficiency. *E. coli*, *S. aureus*, *Bacillus subtilis* (*B. subtilis*), and *Rhizoctonia solani* (*R. solani*) were chosen as representatives of gram-negative bacteria, gram-positive bacteria, and fungi, respectively, to evaluate the broad-spectrum antibacterial action of CNQDs [Figure 6B]. For comparison, three types of g-C_3N_4 with varying N_V contents were prepared, and experimental data demonstrated that CNQDs with more N_V exhibited higher POD-like activity. Coupled with their diffusion capability, CNQDs could penetrate the interior of bacteria and fungi, enhancing bacterial binding affinity and overcoming the inherent drawbacks of short ROS lifetimes and limited diffusion distances. This work underscores the enormous potential of CNQDs as highly efficient antibacterial agents[25]. Furthermore, leveraging the abundant "N reservoir" in g-C_3N_4 analogous to the enzyme protein portion, which acts as an effective "claw" to anchor metal atoms, they reported a self-cleaving method to prepare atomically thin single-atom nanodots (NDs). These NDs closely mimic the natural enzyme structure, exhibiting excellent POD-like activity and antibacterial efficacy. To further enhance the enzyme-mimetic catalytic activity and antibacterial effects of g-C_3N_4-based nanomaterials, Cu single-atom-doped g-C_3N_4 NDs (Cu-CNNDs) were

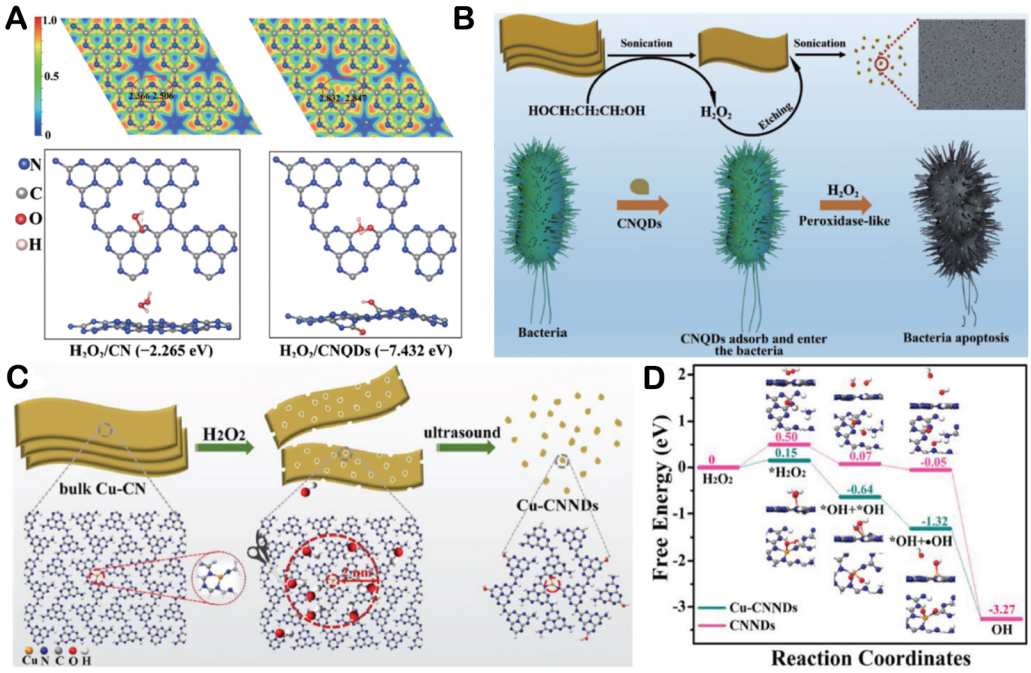

Figure 6. (A) ELF and the structure models and adsorption energy values for absorbing H_2O_2 based on DFT calculation of CN and CNQDs. (B) Schematic illustration of the strategy for the preparation of CNQDs with NVs in propylene glycol under sonication: CNQDs can efficiently kill bacteria by binding to bacteria through cellular internalization and simultaneously generating ROS by their POD-like catalysis. (Reproduced with permission[25]. Copyright 2023, Springer Nature). (C) Schematic illustration of the self-tailoring strategy for the preparation of atomically thin Cu-CNNDs. (D) Energy profile diagram for H_2O_2 reduction on CNNDs and Cu-CNNDs. The blue, gray, red, white, and orange balls refer to the N, C, O, H, and Cu atoms, respectively. (Reproduced with permission[103]. Copyright 2023, Wiley-VCH).

prepared using a self-cleaving strategy [Figure 6C]. Due to the size effects of the carrier optimizing the coordination structure, this led to the complete exposure of Cu-N_3 active sites, enhancing the ability to generate •OH from H_2O_2 [Figure 6D]. Through covalent grafting, these Cu-CNNDs were stably loaded onto cotton textiles, resulting in the formation of a composite antibacterial cotton textile[103].

Synergistic sterilization

Through the modification of g-C_3N_4 nanomaterials, the augmentation of photocatalytic activity is not only attainable, but the material can also acquire enzymatic catalytic features. This modification facilitates more effective sterilization through synergistic interactions[104].

Zhang *et al.* revealed the exceptional enzymatic attributes of g-C_3N_4 following modification with KOH and KCl (AKCN) [Figure 7A]. This tailored material exhibits a unique resemblance to the enzymatic interplay of glucose oxidase-POD [Figure 7B]. Under illuminated conditions, a cascade of catalytic reactions ensues, rendering it well-suited for glucose detection. The adapted g-C_3N_4 demonstrates glucose oxidase-like prowess, orchestrating the catalysis of glucose oxidation and O_2 reduction under visible light exposure. This process yields H_2O_2 with an extraordinary apparent quantum efficiency nearing 100%. Interestingly, the material also exhibits POD-like activity, facilitating the breakdown of locally generated H_2O_2 in darkness while simultaneously oxidizing the initially colorless substrate 3,3',5,5'-tetramethylbenzidine (TMB), ultimately enabling comprehensive glucose detection. Utilizing this nanozyme design, a microfluidic device achieves rapid blood glucose level detection within a mere 30 s, featuring an impressive minimum detection limit of 0.8 μM[105]. In a parallel investigation, Wang *et al.* devised a dual-functional material, S-doped

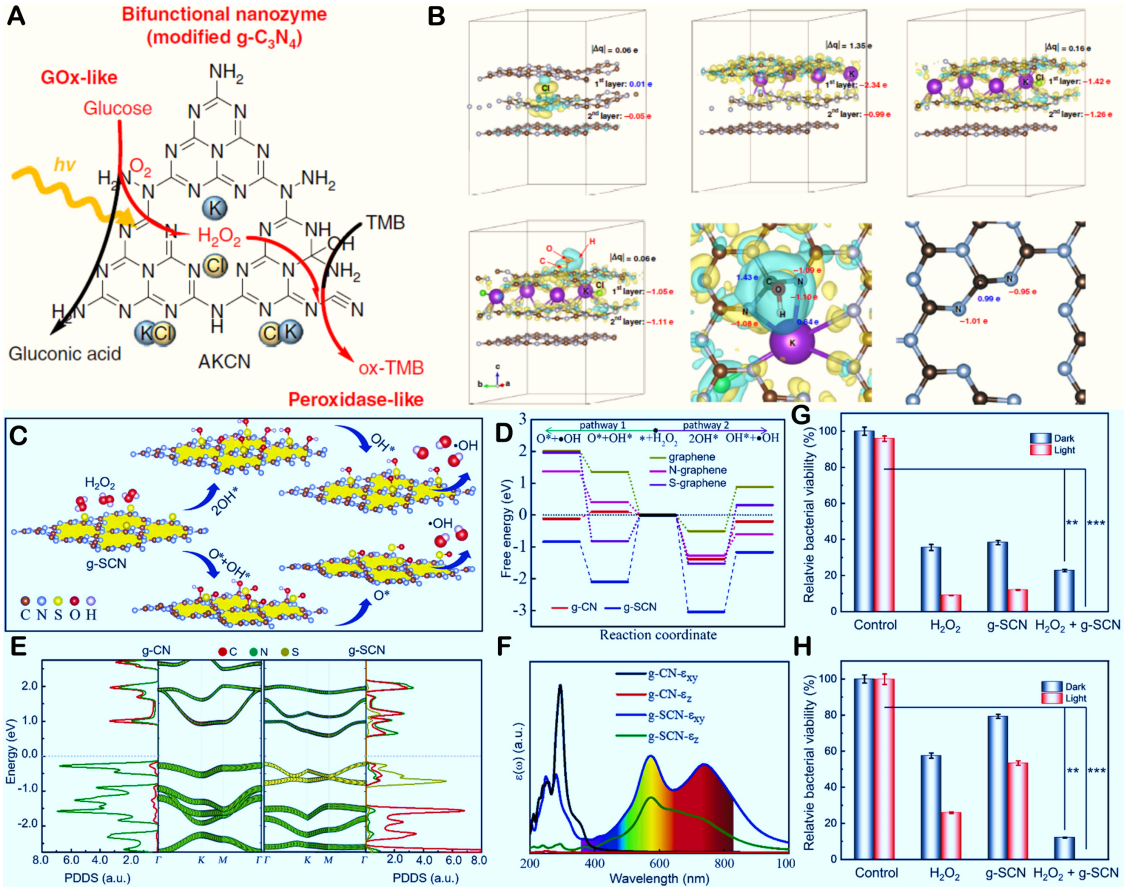

Figure 7. (A) Glucose detection using a synthetic bifunctional nanozyme: photocatalytic aerobic oxidation of glucose with *in situ* production of H_2O_2 on AKCN. (B) Charge distribution analysis from DFT calculations. (Reproduced with permission[105]. Copyright 2019, Springer Nature). (C) The intermediates during the H_2O_2 decomposition process. (D) The free energy diagrams of the different models for the production of catalyst hydroxyl radical. (E) Orbital-resolved band structures of g-CN and g-SCN lattices. The red, green, and yellow dots represent the contributions from C, N, and S atoms. The energy at the Fermi level was set to zero. (F) Imaginary parts of dielectric constant for g-C_3N_4 and g-SCN, respectively. (G and H) Relative survival rate of bacteria for Chl^r *E. coli* (G) and MRSA (H) determined by plate count method under different conditions. (Reproduced with permission[26]. Copyright 2023, Elsevier).

g-C_3N_4, endowed with both photocatalytic and enzymatic activities through S incorporation into g-C_3N_4. S doping not only amplifies the absorption spectrum of the material but also enhances its photocatalytic efficacy [Figure 7C-F][26]. The introduction of S establishes S-N-C bonds, conferring enzymatic activity upon the material. Leveraging the collaborative influence of photocatalysis and enzymatic catalysis, the synergistic process generates an increased abundance of ROS [Figure 7G and H][26].

PRACTICAL APPLICATION OF g-C_3N_4-BASED MATERIALS IN ANTIBACTERIAL

Water purification

In the natural milieu, the bacterial population in one milliliter of pristine water typically registers below 100, whereas heavily contaminated aquatic environments may surpass one million bacteria per milliliter. The introduction of pathogenic microorganisms into water bodies poses the risk of widespread infectious diseases, including cholera, typhoid fever, poliomyelitis, hepatitis A, and bacterial dysentery. The global scarcity of clean water resources presents a formidable challenge. Researchers worldwide are actively investigating diverse methodologies to discover an efficient and energy-conserving catalytic material for the proficient disinfection of water. Non-metallic photocatalysts, with g-C_3N_4 materials as a prominent example,

boast several advantages such as cost-effectiveness and high resistance to acidic and alkaline conditions. Significantly, they have the capacity to thwart secondary pollution stemming from the leaching of metals into water. This category of catalysts is viewed as an exceptionally promising and groundbreaking solution to address the urgent demand for clean water resources on a global scale.

Li *et al*. devised a composite photocatalyst, g-C_3N_4/Ag_2WO_4, employing a synthesis method that combined thiourea and ammonium chloride through polymerization and precipitation [Figure 8A and B]. This innovative photocatalyst demonstrated exceptional efficacy under visible light for the deactivation of *E. coli*. The Ag_2WO_4 particles exhibited uniform dispersion on the g-C_3N_4 surface, optimizing the separation of photoinduced electron-hole pairs through a synergistic interplay with g-C_3N_4 [Figure 8C]. Notably, the synthesized photocatalyst outperformed pure g-C_3N_4 and Ag_2WO_4, showcasing significantly heightened disinfection efficiency under visible light conditions [Figure 8D][106].

Teng *et al*. engineered g-C_3N_4 NSs by modifying their edges, facilitating the efficient separation of electrons and holes. Simultaneously, this edge modification enhanced the adsorption of oxygen molecules on the nanomaterial, consequently promoting the generation of oxygen-containing species with potent bactericidal properties [Figure 8E]. In comparison to catalysts known for their peak photocatalytic activity, this material achieved equivalent results with merely one-tenth of the required dosage [Figure 8F]. Impressively, its catalytic prowess rivaled that of the most potent current metal catalysts. Furthermore, the catalyst, when loaded onto a substrate for sterilization, mitigated the diffusion of the catalyst into water. This approach circumvented the need for subsequent separation treatments in drinking water purification, streamlining the purification process and reducing associated costs [Figure 8G]. Moreover, by applying this nanomaterial as a coating on glass or plastic surfaces, a continuous and efficient water purification device was devised [Figure 8H]. Contaminated sewage entered the device from the inlet, swiftly achieving sterilization and purification, ultimately yielding potable water at the outlet. In the presence of midday sunlight, bacteria-contaminated water purification was accomplished within a mere 30 min, attaining an impressive sterilization efficiency of 99.9999%[107].

Air purification

Airborne microbial pollution represents a facet of environmental degradation and emerges as a pivotal contributor to infectious diseases. Presently, 20% of respiratory illnesses can be traced back to the influence of airborne microbial pollution. Of the 41 globally predominant infectious diseases, a noteworthy 14 are instigated by the transmission of microbes through the air. Notably, recent years have witnessed the correlation between major public health crises - such as the occurrences of SARS, H1N1, avian influenza, hand-foot-and-mouth disease, and the emergence of superbugs - and microbial contamination.

Many commercially available air purification systems depend on dense fiber filtration membranes to trap bioaerosols. These filters typically function based on the pore size of the filtration membrane, utilizing the size-exclusion effect for bioaerosol capture. However, such filters often feature small pore sizes, resulting in elevated pressure drops, susceptibility to clogging, and a lack of antibacterial functionality. Addressing these challenges, Peng *et al*. have conceived and engineered a dual-functional bioaerosol filter incorporating a double-layered foam Ni material loaded with CT and modified with polydopamine (PDA) (CT/Ni-PDA/Ni) [Figure 9A]. Under high airflow conditions of 12.5 L min^{-1}, this dual-functional bioaerosol filter attains a remarkable removal efficiency of 93.5% for bioaerosols, accompanied by a mere 1,000 Pa pressure drop [Figure 9B and C]. Concurrently, the continuous inactivation efficiency reaches 70.0%. Furthermore, extended irradiation time and heightened light intensity elevate the bioaerosol inactivation rate to an impressive 99.99%. Experimental findings suggest that the non-size-dependent capture effect of this bioaerosol filter is ascribed to the combined adhesive force and charge facilitated by PDA [Figure 9D].

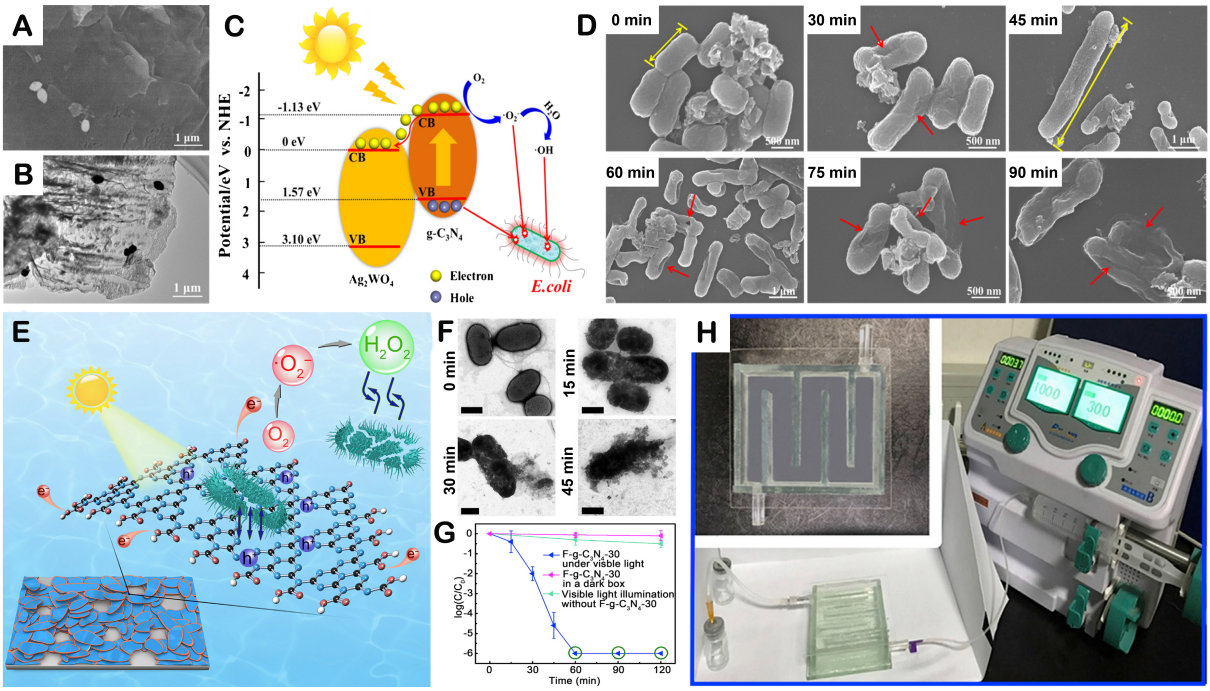

Figure 8. (A and B) scanning electron microscope (SEM) and transmission electron microscope (TEM) images of C_3N_4/Ag_2WO_4 heterostructure. (C) Mechanism of photocatalytic disinfection treated with C_3N_4/Ag_2WO_4 heterostructure under visible light irradiation. (D) SEM images of *E. coli* (10^7 CFU/mL) treated with C_3N_4/Ag_2WO_4 heterostructure under visible light irradiation for different times. The red arrows indicate deformation, pore-forming, and fracture of *E. coli* cells. The yellow double arrows indicate the length of *E. coli* cells. (Reproduced with permission[106]. Copyright 2017, Elsevier). (E) Schematic diagram of indirect bacteria inactivation using H_2O_2 generated by an edge-functionalized g-C_3N_4 nanosheet. (F) TEM images of *E. coli* (D) before and after irradiation for different times. Each scale bar represents 500 nm (G). (A) Comparison of the disinfection performances of F-g-C_3N_4-30 with control experiments. (H) Disinfection devices based on F-g-C_3N_4-30-EP: Photograph of newly prepared F-g-C_3N_4-30-EP-modified polyethylene bag filled with water. (Reproduced with permission[107]. Copyright 2019, Elsevier).

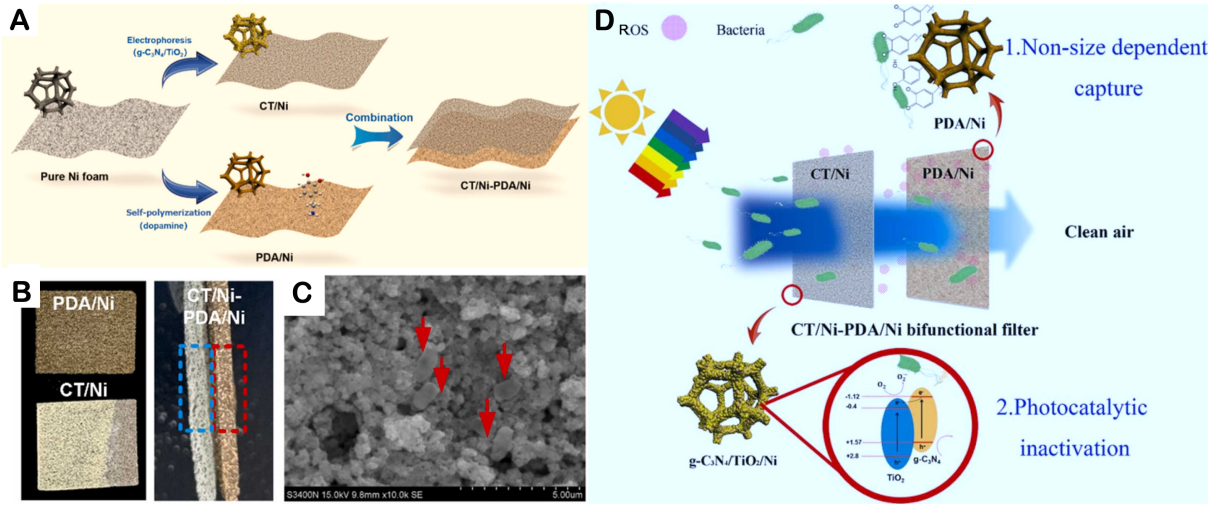

Figure 9. (A) Illustration of preparation procedure of the CT/Ni-PDA/Ni. (B) Digital images of the CT/Ni-PDA/Ni. (C) SEM image of the bacteria captured by the CT/Ni. (D) Photocatalytic inactivation of airborne bacteria onto CT/Ni-PDA/Ni bifunctional coupling filter with non-size dependent capture effect. (Reproduced with permission[108]. Copyright 2023, Elsevier).

Additionally, a co-detection method using Raman spectroscopy in conjunction with chemiluminescence verifies the production and transmission of photocatalytic ROS in the air, playing a pivotal role in bioaerosol inactivation. This groundbreaking research holds the potential to introduce innovative strategies for the development of dual-functional filters capable of capturing and photocatalytically deactivating bioaerosols in a size-independent manner[108].

Treatment of bacterial infections

In recent years, heightened attention has been directed toward both individual and public health events associated with microbial infections. The predominant method for addressing bacterial infections involves the application of antibiotics; however, the excessive use of these antibiotics has given rise to the emergence of antibiotic-resistant "superbugs", presenting a significant menace to both public health and the environment. The exploitation of the catalytic attributes inherent in g-C_3N_4 nanomaterials, enabling the generation of ROS for antibacterial treatment, offers a spectrum of advantages, including broad-spectrum activity, heightened stability, cost-effectiveness, and the absence of contribution to bacterial resistance. This innovative approach is swiftly gaining recognition as a promising therapeutic method.

Wang *et al.* successfully crafted an entirely organic composite photocatalytic nanomaterial, denoted as the g-C_3N_4/perylene-3,4,9,10-tetracarboxylic diimide (PDINH) heterostructure, through the *in situ* recrystallization of PDINH on the g-C_3N_4 surface [Figure 10A and B]. The absorption spectrum of this innovative composite spans from UV to NIR light (750 nm). The formation of the heterostructure facilitates efficient separation of charge carriers, resulting in remarkably high photocatalytic efficiency. The heightened photocatalysis generates an increased quantity of ROS, showcasing exceptional bactericidal effects against both Gram-negative and Gram-positive bacteria. Notably, owing to the absence of metallic elements, the material exhibits minimal toxicity to normal tissue cells. Moreover, when applied to treat infected wounds, it significantly enhances wound regeneration in mouse wounds infected with *Streptococcus mutans (S. aureus)* [Figure 10C][109].

Peng *et al.* employed polyphosphoric acid (PPA) as a solvent for dispersing g-C_3N_4. This non-oxidizing solvent, gentler in comparison to concentrated sulfuric acid and methylsulfonyl chloride [Figure 10D], was chosen for the dispersion of g-C_3N_4. Through a combination of experiments and theoretical calculations, a comprehensive mechanism for the dissolution of g-C_3N_4 was proposed, encompassing protonation intercalation, adsorption energy, and viscosity shear force. Identification of commercial ionic liquids meeting specified criteria validated the universal applicability of this mechanism for achieving the dissolution of pCN. Leveraging its mild nature and excellent dispersibility towards carbon nanotubes (CNTs), a pCN/CNT nanocomposite film was facilely prepared through co-dissolution, co-precipitation, and filtration [Figure 10E and F]. Exploiting robust π-π interface interactions, pCN tightly envelops the surface of bundled CNTs, markedly enhancing the mechanical properties of the resulting flexible pCN film. This enhancement plays a pivotal role in bolstering the durability of the pCN film under operational conditions [Figure 10G]. When applied to treat mouse wounds infected with *S. aureus*, the pCN/CNT film demonstrated exceptional efficacy in accelerating wound closure, yielding smaller wounds compared to those treated with conventional gauze under sunlight [Figure 10H]. Subsequent experiments involving HE and Masson staining substantiated that wounds treated with the pCN/CNT film exhibited reduced inflammation, wider collagen distribution, and increased new blood vessels compared to control gauze, confirming the positive impact of the pCN/CNT film on wound healing [Figure 10I][110].

Guo *et al.* employed a covalent grafting approach to link adenine amine (ADN) onto g-C_3N_4, resulting in ADN-grafted g-C_3N_4 (g-C_3N_4/ADN) NSs [Figure 10J]. The resulting g-C_3N_4/ADN exhibited a narrow

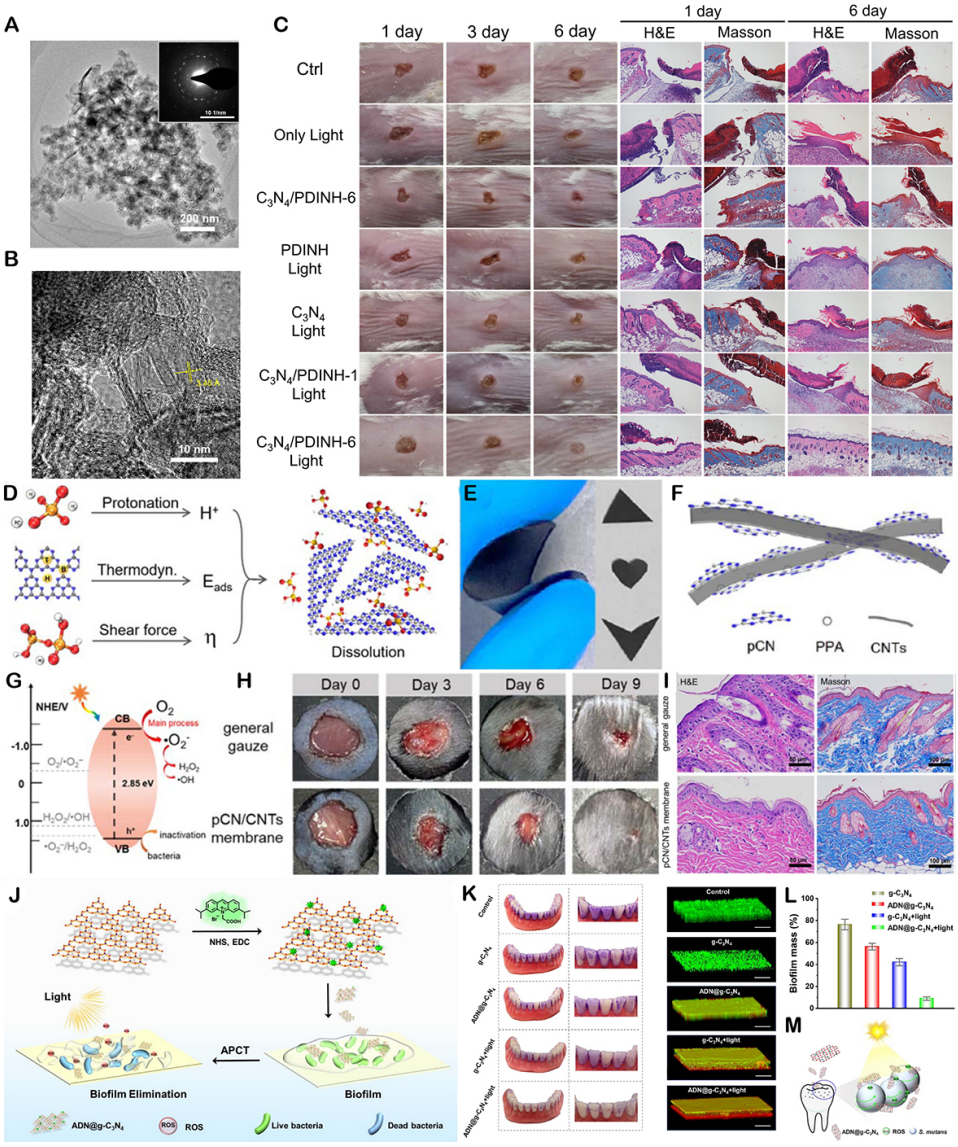

Figure 10. (A and B) TEM images of g-C_3N_4/PDINH heterostructures. (C) Photographs of the infected wound treated in different days and the infected wound histologic analyses in day 1 and day 6 with different treatments. The scale bar in the photographs is 0.5 cm and, in the histologic picture, is 100 μm. (Reproduced with permission[109]. Copyright 2019, Wiley-VCH). (D) Proposed pCN dissolution mechanism. (E) Photographs of the as-prepared free-standing pCN/CNT membrane, 180° folded profile, and tailored ones of different shapes. (F) Scheme of pCN and CNTs in the composite membrane. (G) Energy band position of g-C_3N_4 on the pCN/CNT membrane with respect to ROS formation potential. (H) Photographs of *S. aureus*-infected wounds in laboratory mice treated with the pCN/CNT membrane and control gauze at different times. (I) Histologic analysis (HE, Masson, CD31) of the *S. aureus*-infected wounds after treatment with the pCN/CNT membrane and control gauze for nine days. (Reproduced with permission[110]. Copyright 2023, Royal Society of Chemistry). (J) Scheme illustrated the synthesis of g-C_3N_4/ADN and corresponding bacterial killing and biofilm elimination activities. Eradication of mature *S. mutans* biofilm by the synthesized NSs. (K) Pictures of 48 h mature *S. mutans* biofilm on tooth models incubated with PBS, g-C_3N_4, g-C_3N_4/ADN, g-C_3N_4 + light, and g-C_3N_4/ADN + light. (L) Remaining biofilm biomass determined by CV staining after 3 h of incubation. (M) Scheme illustrates the antibacterial mechanism of g-C_3N_4/ADN. (Reproduced with permission[111]. Copyright 2022, Elsevier).

optical bandgap and a broad light absorption spectrum spanning from UV to NIR regions. Under illumination, g-C_3N_4/ADN generated ROS, manifesting effective bactericidal and biofilm elimination effects against both Gram-negative and Gram-positive bacteria [Figure 10K]. Molecular dynamics simulations elucidated that g-C_3N_4/ADN could orient, adhere to, and insert into bacterial lipid bilayers through strong

van der Waals and electrostatic interactions, thereby reducing lipid order and enhancing the conductivity of ROS migration. This induced improved antibacterial and anti-biofilm properties in g-C_3N_4/ADN [Figure 10L]. Consequently, g-C_3N_4/ADN efficiently eradicated oral biofilms on artificial teeth surfaces [Figure 10M]. This pioneering work introduces a potential broad-spectrum light-induced photocatalytic therapy for the prevention and treatment of plaque-related diseases and infections associated with artificial teeth, showcasing its promising applications in tackling resilient biofilms[111].

Self-cleaning film

The antimicrobial attributes inherent in C_3N_4-based nanomaterials have been harnessed for the development of self-cleaning thin films. Ma *et al.* adeptly applied a proprietary technique involving a g-C_3N_4 NS coating on Cu_xP through a non-solvent-induced phase separation approach. This innovative method yielded PVDF-CTFE mixed matrix membranes (PVDF-CTFE MMMs) endowed with both antibacterial and self-cleaning functionalities, achieved through the incorporation of g-C_3N_4/Cu_xP as a tailored additive. The robust affinity between Cu_xP and g-C_3N_4 NSs serves a dual purpose: safeguarding copper against oxidation and facilitating the transfer of photogenerated electrons. This synergistic effect enhances the photocatalytic prowess of the NSs, elevating the fouling resistance of PVDF-CTFE membranes. Moreover, co-blending modification imparts superior mechanical properties, permeability, and ultrafiltration performance to the membrane, as reported in a manner befitting the standards of Nature journal[112].

Chen *et al.* have innovatively crafted a state-of-the-art graphene-based membrane employing a hybrid assembly approach. This pioneering membrane integrates Ag NPs tethered to g-C_3N_4 (Ag@g-C_3N_4), serving as both pillars and photocatalysts [Figure 11A]. The uniform deposition of Ag on g-C_3N_4 markedly amplifies its photocatalytic prowess. Concurrently, it establishes additional water transport channels amidst reduced graphene oxide (rGO) and g-C_3N_4 layers. The resultant rGO/Ag@g-C_3N_4 nanofiltration membrane showcases superior water permeability, exceptional photocatalytic self-cleaning efficacy, remarkable flexibility, and structural stability when juxtaposed with pristine rGO membranes characterized by larger interlayer spacing and rugged surfaces. Following a one-hour exposure to visible light, the reversible decline in flux attributed to pollutant molecule adsorption attains an extraordinary flux recovery rate of 98.1%. Moreover, the elevated flux of the rGO/Ag@g-C_3N_4 membrane remains steadfast in a cross-flow photocatalytic nanofiltration apparatus[113].

In a parallel study, Xiong *et al.* have engineered antibacterial cotton featuring heterojunction structures of CT on the surface of natural cotton [Figure 11B]. Upon solar irradiation-induced excitation of g-C_3N_4 and TiO_2, electron-hole pairs are generated. Simultaneously, electrons from g-C_3N_4 migrate to the CB of TiO_2. Photogenerated electrons on the g-C_3N_4 CB may interact with O_2, yielding $\bullet O_2^-$. Concurrently, photogenerated holes on the TiO_2 VB may react with H_2O or •OH, potentially producing •OH. The utilization of these generated free radicals achieves highly effective antibacterial outcomes[114]. Furthermore, Li *et al.* have achieved self-cleaning and antibacterial attributes in a membrane by facilely depositing g-C_3N_4 NSs onto a porous polyacrylonitrile (PAN) substrate [Figure 11C]. The peeled-off g-C_3N_4 NSs manifest a graphite-like morphology with numerous undulations and grooves, furnishing additional active sites conducive to photocatalytic reactions. The antimicrobial efficacy of the g-C_3N_4 NS membrane was evaluated against *E. coli*, demonstrating exceptional antibacterial effects [Figure 11D-G][115].

SUMMARY AND PERSPECTIVE

Currently, significant progress has been made in the exploration of g-C_3N_4-based materials for antibacterial applications, encompassing synthesis, mechanistic elucidation, and a broad spectrum of application areas. This comprehensive review meticulously elucidates the structure, characteristics, and preparation methods

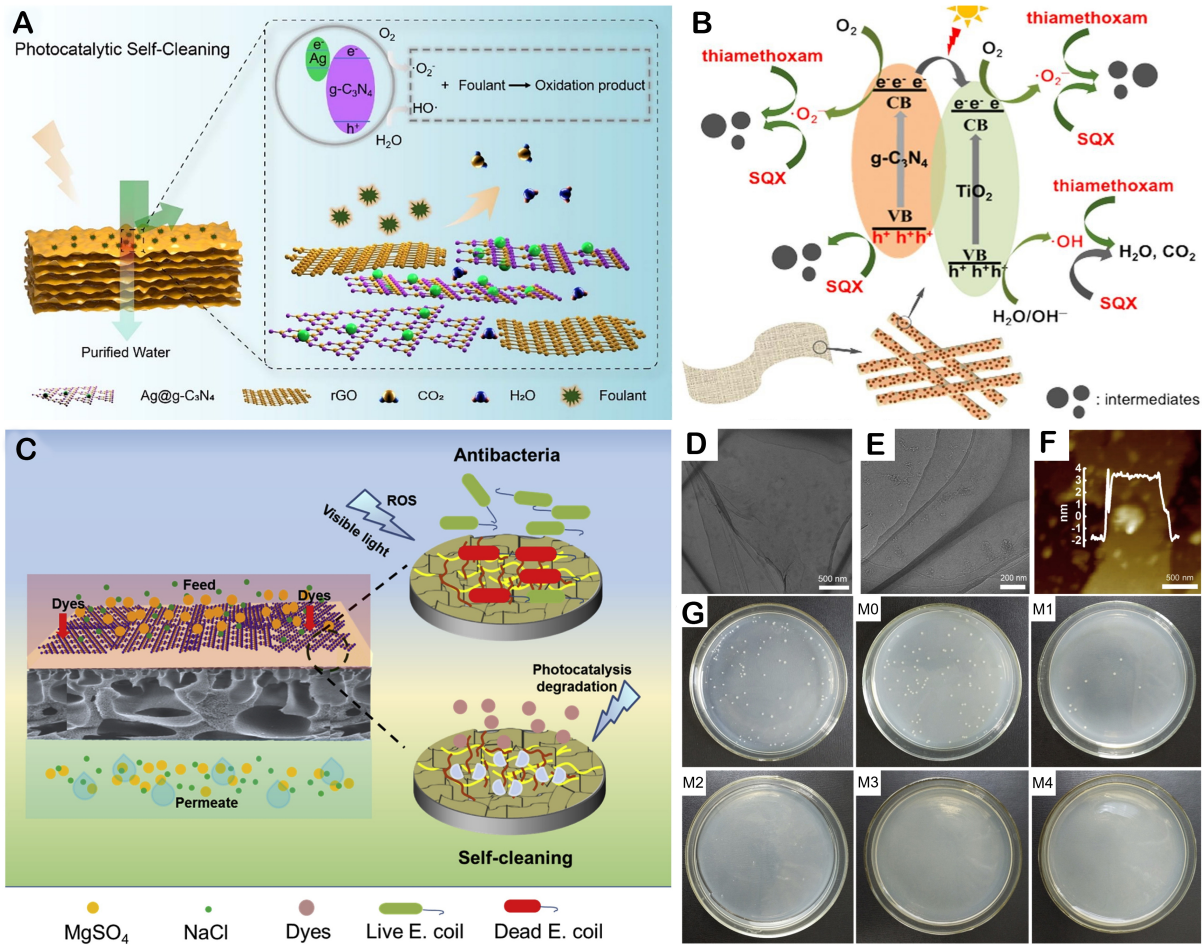

Figure 11. (A) Self-cleaning mechanism of g-C_3N_4/Ag/rGO membrane under visible light irradiation. (Reproduced with permission[113]. Copyright 2022, Elsevier). (B) Possible photocatalytic mechanism for CT g-C_3N_4/TiO_2-cotton under solar irradiation. (Reproduced with permission[114]. Copyright 2021, Elsevier). (C) The proposed mechanisms of g-C_3N_4 NS membranes. (D and E) TEM images of the g-C_3N_4 NSs at different magnifications and (F) AFM images of g-C_3N_4 NSs. (G) Antimicrobial activities against *E. coli* of g-C_3N_4 membranes at different ratios. (Reproduced with permission[115]. Copyright 2019, Elsevier).

of g-C_3N_4, paving the way for innovative applications by providing an in-depth understanding of its distinctive properties. The sterilization mechanisms of g-C_3N_4 are expounded upon, spanning from physical structure sterilization to the intricate realms of photocatalytic and enzymatic antibacterial activities. g-C_3N_4 exhibits a diverse repertoire of antibacterial mechanisms, with a specific emphasis on synergistic effects, thereby accentuating the potential for heightened antibacterial efficacy through strategic amalgamation of these mechanisms. Lastly, practical applications of photocatalytic antibacterial properties are introduced, showcasing the adaptability of g-C_3N_4-based nanomaterials across diverse environments, including water and air purification, bacterial infection treatment, and the development of self-cleaning film. Table 1 is devoted to offering contemporary perspectives on the antibacterial mechanisms and applications of nanomaterials based on g-C_3N_4-based nanomaterials. Looking into the future, this field harbors vast potential for extensive exploration and groundbreaking innovation.

High-efficiency large-scale synthesis methods

Future investigations may be dedicated to the development of more efficient and controllable synthesis methodologies, allowing for precise modulation of the structure and properties of g-C_3N_4. The introduction

Table 1. Summary of g-C_3N_4-based nanomaterials and their antimicrobial applications

Materials	Activities	Applications	Preference	Ref.
Ag/g-C_3N_4	Nanozyme bacteria-killing	Treatment of bacterial infections	*In vitro*: break down the biofilms and prevent formation of new biofilms *In vivo*: prevent bacterial infections and accelerate the healing rate of wounds	[99]
g-C_3N_4	Photocatalytic bacteria-killing	Water purification	Inactivation of *E. coli* K-12	[15]
g-C_3N_4/PDINH	Photocatalytic bacteria-killing	Treatment of bacterial infections	Efficient promotion of infectious wound regeneration in mice with *S. aureus*-infected dermal wounds is demonstrated	[109]
pCN/CNTs	Photocatalytic bacteria-killing	Treatment of bacterial infections	Excellent photocatalytic sterilization and wound healing capacity both *in vitro* and *in vivo*	[110]
ADN@g-C_3N_4	Photocatalytic bacteria-killing	Treatment of bacterial infections	Effectively eradicate oral biofilm on artificial teeth surfaces	[111]
g-SCN	Synergistic sterilization	Treatment of bacterial infections	Successfully applied to mice that were treated for wound infection	[26]
g-C_3N_4/TiO_2	Photocatalytic bacteria-killing	Air purification	Explored for bioaerosols capture and photocatalytic inactivation	[108]
N-g-C_3N_4	Physical bacteria-killing	Water purification	Higher hydrophilicity and aqueous solubility, leading to a high broad-spectrum antibacterial activity	[79]
Ag@g-C_3N_4	Photocatalytic bacteria-killing	Self-cleaning film	Excellent photocatalytic self-cleaning ability	[113]
g-C_3N_4	Photocatalytic bacteria-killing	Self-cleaning film	Excellent water permeability and good antibacterial activity	[115]
CNDQs	Nanozyme bacteria-killing	Water purification	The sterilization rate against *E. coli*, *S. aureus*, *B. subtilis*, and *R. solani* reaches more than 99%	[25]
Cu-CNNDs	Nanozyme bacteria-killing	Self-cleaning film	Exhibit over 99% antibacterial efficacy and successfully grafted onto cotton fabrics	[103]
Ag_2WO_4/g-C_3N_4	Photocatalytic bacteria-killing	Water purification	Exhibited outstandingly enhanced photocatalytic disinfection efficiency	[106]
g-C_3N_4	Photocatalytic bacteria-killing	Water purification	Rapidly purified in 30 min with a disinfection efficiency of over 99.9999% under visible-light irradiation	[107]
Cu_xP@g-C_3N_4	Photocatalytic bacteria-killing	Self-cleaning film	Excellent antibacterial activity and self-cleaning ability	[112]
CeO_2/PCN	Photocatalytic bacteria-killing	Water purification	The sterilization rate towards *S. aureus* under visible-light irradiation could be up to 88.1%	[96]

of innovative synthetic strategies holds the potential to further enhance the antibacterial performance of nanomaterials. The exploration of novel synthesis approaches and the scaling up of production processes are anticipated to streamline the practical deployment of materials based on g-C_3N_4.

Elucidating antibacterial mechanism

Acquiring a comprehensive comprehension of the antibacterial mechanisms intrinsic to g-C_3N_4-based nanomaterials is paramount, with a specific focus on aspects such as physical structure sterilization, photocatalytic antibacterial processes, nanozyme antibacterial activities, and synergistic effects. This investigative endeavor is poised to furnish profound scientific insights that will significantly inform the future design and optimization of highly targeted and efficient antibacterial materials. The outcomes of these studies are anticipated to unveil the latent application value of g-C_3N_4 materials within the realm of antibacterial research, presenting substantive solutions to tackle challenges presented by diverse bacterial strains.

Investigation of toxicity

As nanomaterials, their toxicity is a complex issue that has existed for a long time and is influenced by multiple factors. At present, g-C_3N_4 exhibits good biocompatibility, but the chemical composition,

morphology, size, and surface properties of its composite materials can all affect its toxicity. How to reduce toxicity and potential side effects remains to be further studied and answered.

Expanding application areas

g-C_3N_4-based antibacterial materials have shown great potential in fields such as water treatment, air purification, treatment of bacterial infections, and self-cleaning films. However, most applications are still in the prototype stage, and further practical application is our development direction. In addition, expanding the application of g-C_3N_4-based antibacterial materials in food packaging, kitchenware, hospital towels, quilts, and other fields is quite important. These efforts are essential to guarantee the sustainable utilization of these materials in antibacterial applications.

In summary, the trajectory from synthesis to the pragmatic application of g-C_3N_4-based materials in the realm of antibacterial research epitomizes a dynamic and auspicious developmental pathway. Sustained research endeavors and interdisciplinary collaboration will be pivotal in fully unlocking the potential of g-C_3N_4 and propelling innovations that effectively tackle antibacterial challenges across diverse domains.

DECLARATIONS

Authors' contributions

Conceptual design and project supervision: Yu X
Manuscript draft and revision: Zhang X, Wu X, Zhang J, Xu H

Availability of data and materials

Not applicable.

Financial support and sponsorship

This work was supported by the Taishan Scholar Project of Shandong Province (No. tsqn202211168), the National Natural Science Foundation of China (No. 52272212), the Natural Science Foundation of Shandong Province (No. ZR2022JQ20), and the Key Laboratory of Optic-electric Sensing and Analytical Chemistry for Life Science, MOE (No. M2022-7).

Conflicts of interest

All authors declared that there are no conflicts of interest.

Ethical approval and consent to participate

Not applicable.

Consent for publication

Not applicable.

REFERENCES

1. Janik E, Ceremuga M, Niemcewicz M, Bijak M. Dangerous pathogens as a potential problem for public health. *Medicina* 2020;56:591. DOI PubMed PMC
2. Uddin TM, Chakraborty AJ, Khusro A, et al. Antibiotic resistance in microbes: history, mechanisms, therapeutic strategies and future prospects. *J Infect Public Health* 2021;14:1750-66. DOI
3. Serwecińska L. Antimicrobials and antibiotic-resistant bacteria: a risk to the environment and to public health. *Water* 2020;12:3313. DOI

4. Ukuhor HO. The interrelationships between antimicrobial resistance, COVID-19, past, and future pandemics. *J Infect Public Health* 2021;14:53-60. DOI PubMed PMC
5. Wang Y, Yang Y, Shi Y, Song H, Yu C. Antibiotic-free antibacterial strategies enabled by nanomaterials: progress and perspectives. *Adv Mater* 2020;32:e1904106. DOI
6. Wang L, Tang X, Yang Z, et al. Regulation of functional groups enable the metal-free PDINH/GO advisable antibacterial photocatalytic therapy. *Chem Eng J* 2023;451:139007. DOI
7. Wang L, Liu L, You Z, et al. Surface amorphization oxygen vacancy-rich porous Sn_3Ox nanosheets for boosted photoelectrocatalytic bacterial inactivation. *Rare Met* 2023;42:1508-15. DOI
8. Ong WJ, Tan LL, Ng YH, Yong ST, Chai SP. Graphitic carbon nitride (g-C_3N_4)-based photocatalysts for artificial photosynthesis and environmental remediation: are we a step closer to achieving sustainability? *Chem Rev* 2016;116:7159-329. DOI
9. Iqbal O, Ali H, Li N, et al. A review on the synthesis, properties, and characterizations of graphitic carbon nitride (g-C_3N_4) for energy conversion and storage applications. *Mater Today Phys* 2023;34:101080. DOI
10. Wang J, Wang S. A critical review on graphitic carbon nitride (g-C_3N_4)-based materials: preparation, modification and environmental application. *Coord Chem Rev* 2022;453:214338. DOI
11. Yu Y, Yan W, Wang X, et al. Surface engineering for extremely enhanced charge separation and photocatalytic hydrogen evolution on g-C_3N_4. *Adv Mater* 2018;30:1705060. DOI
12. Cao S, Yu J. g-C_3N_4-based photocatalysts for hydrogen generation. *J Phys Chem Lett* 2014;5:2101-7. DOI PubMed
13. Wang X, Maeda K, Thomas A, et al. A metal-free polymeric photocatalyst for hydrogen production from water under visible light. *Nat Mater* 2009;8:76-80. DOI
14. Yu Y, Wang J. Direct microwave synthesis of graphitic C_3N_4 with improved visible-light photocatalytic activity. *Ceram Int* 2016;42:4063-71. DOI
15. Huang J, Ho W, Wang X. Metal-free disinfection effects induced by graphitic carbon nitride polymers under visible light illumination. *Chem Commun* 2014;50:4338-40. DOI PubMed
16. Thurston JH, Hunter NM, Wayment LJ, Cornell KA. Urea-derived graphitic carbon nitride (u-g-C_3N_4) films with highly enhanced antimicrobial and sporicidal activity. *J Colloid Interface Sci* 2017;505:910-8. DOI PubMed PMC
17. Khan ME, Han TH, Khan MM, Karim MR, Cho MH. Environmentally sustainable fabrication of Ag@ g-C_3N_4 nanostructures and their multifunctional efficacy as antibacterial agents and photocatalysts. *ACS Appl Nano Mater* 2018;1:2912-22. DOI
18. Sun L, Du T, Hu C, et al. Antibacterial activity of graphene Oxide/g-C_3N_4 composite through photocatalytic disinfection under visible light. *ACS Sustain Chem Eng* 2017;5:8693-701. DOI
19. Aquino de Carvalho N, Wang Y, Morales-soto N, et al. Using C-doping to identify photocatalytic properties of graphitic carbon nitride that govern antibacterial efficacy. *ACS EST Water* 2021;1:269-80. DOI
20. Mirzaei H, Darroudi M. Zinc oxide nanoparticles: biological synthesis and biomedical applications. *Ceram Int* 2017;43:907-14. DOI
21. Sirelkhatim A, Mahmud S, Seeni A, et al. Review on zinc oxide nanoparticles: antibacterial activity and toxicity mechanism. *Nanomicro Lett* 2015;7:219-42. DOI PubMed PMC
22. Sundaram IM, Kalimuthu S, Ponniah G. Highly active ZnO modified g-C_3N_4 nanocomposite for dye degradation under UV and visible light with enhanced stability and antimicrobial activity. *Compos Commun* 2017;5:64-71. DOI
23. Qamar MA, Shahid S, Javed M, Iqbal S, Sher M, Akbar MB. Highly efficient g-C_3N_4/Cr-ZnO nanocomposites with superior photocatalytic and antibacterial activity. *J Photoch Photobio A Chem* 2020;401:112776. DOI
24. Qamar MA, Shahid S, Javed M, et al. Fabricated novel g-C_3N_4/Mn doped ZnO nanocomposite as highly active photocatalyst for the disinfection of pathogens and degradation of the organic pollutants from wastewater under sunlight radiations. *Colloid Surface A Physicochem Eng Asp* 2021;611:125863. DOI
25. Dai X, Liu H, Du W, et al. Biocompatible carbon nitride quantum dots nanozymes with high nitrogen vacancies enhance peroxidase-like activity for broad-spectrum antibacterial. *Nano Res* 2023;16:7237-47. DOI
26. Wang L, Yang Z, Song G, et al. Construction of S-N-C bond for boosting bacteria-killing by synergistic effect of photocatalysis and nanozyme. *Appl Catal B Environ* 2023;325:122345. DOI
27. Mishra A, Mehta A, Basu S, Shetti NP, Reddy KR, Aminabhavi TM. Graphitic carbon nitride (g-C_3N_4)-based metal-free photocatalysts for water splitting: a review. *Carbon* 2019;149:693-721. DOI
28. Tian B, Ho D, Qin J, et al. Framework structure engineering of polymeric carbon nitrides and its recent applications. *Prog Mater Sci* 2023;133:101056. DOI
29. Majdoub M, Anfar Z, Amedlous A. Emerging chemical functionalization of g-C_3N_4: covalent/noncovalent modifications and applications. *ACS Nano* 2020;14:12390-469. DOI
30. Yu F, Wang Z, Zhang S, et al. Molecular engineering of donor-acceptor conjugated polymer/g-C_3N_4 heterostructures for significantly enhanced hydrogen evolution under visible-light irradiation. *Adv Funct Mater* 2018;28:1804512. DOI
31. Yu Y, Cheng S, Wang L, et al. Self-assembly of yolk-shell porous Fe-doped g-C_3N_4 microarchitectures with excellent photocatalytic performance under visible light. *Sustain Mater Technol* 2018;17:e00072. DOI
32. Zhu B, Zhang J, Jiang C, Cheng B, Yu J. First principle investigation of halogen-doped monolayer g-C_3N_4 photocatalyst. *Appl Catal B Environ* 2017;207:27-34. DOI
33. Liu J, Cheng B, Yu J. A new understanding of the photocatalytic mechanism of the direct Z-scheme g-C_3N_4/TiO_2 heterostructure. *Phys Chem Chem Phys* 2016;18:31175-83. DOI

34. Zhu B, Cheng B, Zhang L, Yu J. Review on DFT calculation of *s*-triazine-based carbon nitride. *Carbon Energy* 2019;1:32-56. DOI
35. Chen X, Shi R, Chen Q, et al. Three-dimensional porous g-C_3N_4 for highly efficient photocatalytic overall water splitting. *Nano Energy* 2019;59:644-50. DOI
36. Fu J, Zhu B, Jiang C, Cheng B, You W, Yu J. Hierarchical porous O-doped g-C_3N_4 with enhanced photocatalytic CO_2 reduction activity. *Small* 2017;13:1603938. DOI PubMed
37. Sun J, Zhang J, Zhang M, Antonietti M, Fu X, Wang X. Bioinspired hollow semiconductor nanospheres as photosynthetic nanoparticles. *Nat Commun* 2012;3:1139. DOI
38. Zheng Y, Lin L, Ye X, Guo F, Wang X. Helical graphitic carbon nitrides with photocatalytic and optical activities. *Angew Chem Int Ed* 2014;53:11926-30. DOI
39. Ran J, Ma TY, Gao G, Du X, Qiao SZ. Porous P-doped graphitic carbon nitride nanosheets for synergistically enhanced visible-light photocatalytic H_2 production. *Energy Environ Sci* 2015;8:3708-17. DOI
40. Low J, Yu J, Jaroniec M, Wageh S, Al-Ghamdi AA. Heterojunction photocatalysts. *Adv Mater* 2017;29:1601694. DOI PubMed
41. Kofuji Y, Isobe Y, Shiraishi Y, et al. Carbon nitride-aromatic diimide-graphene nanohybrids: metal-free photocatalysts for solar-to-hydrogen peroxide energy conversion with 0.2% efficiency. *J Am Chem Soc* 2016;138:10019-25. DOI
42. Zhang G, Li G, Lan ZA, et al. Optimizing optical absorption, exciton dissociation, and charge transfer of a polymeric carbon nitride with ultrahigh solar hydrogen production activity. *Angew Chem Int Ed* 2017;56:13445-9. DOI
43. Lin L, Lin Z, Zhang J, et al. Molecular-level insights on the reactive facet of carbon nitride single crystals photocatalysing overall water splitting. *Nat Catal* 2020;3:649-55. DOI
44. Groenewolt M, Antonietti M. Synthesis of g-C_3N_4 nanoparticles in mesoporous silica host matrices. *Adv Mater* 2005;17:1789-92. DOI
45. Gupta A, Bhoyar T, Abraham BM, et al. Potassium molten salt-mediated in situ structural reconstruction of a carbon nitride photocatalyst. *ACS Appl Mater Interfaces* 2023;15:18898-906. DOI
46. Yingsu J, Liu Y, Huang H, et al. Molten-salt synthesis of triazine-based carbon nitride and its photocatalytic degradation mechanism investigation by in situ NMR. *J Phy Chem C* 2023;127:8687-94. DOI
47. Miller TS, Suter TM, Telford AM, et al. Single crystal, luminescent carbon nitride nanosheets formed by spontaneous dissolution. *Nano Lett* 2017;17:5891-6. DOI
48. Ou H, Lin L, Zheng Y, Yang P, Fang Y, Wang X. Tri-*s*-triazine-based crystalline carbon nitride nanosheets for an improved hydrogen evolution. *Adv Mater* 2017;29:1700008. DOI
49. Zhang G, Liu M, Heil T, et al. Electron deficient monomers that optimize nucleation and enhance the photocatalytic redox activity of carbon nitrides. *Angew Chem Int Ed* 2019;58:14950-4. DOI PubMed PMC
50. Guo M, Liu J, Chen X, et al. Graphdiyne oxide nanosheets reprogram immunosuppressive macrophage for cancer immunotherapy. *Nano Today* 2022;45:101543. DOI
51. Guo F, Hu B, Yang C, Zhang J, Hou Y, Wang X. On-surface polymerization of in-plane highly ordered carbon nitride nanosheets toward photocatalytic mineralization of mercaptan gas. *Adv Mater* 2021;33:e2101466. DOI
52. Liang X, Xue S, Yang C, et al. The directional crystallization process of poly (triazine imide) single crystals in molten salts. *Angew Chem Int Ed* 2023;62:e202216434. DOI
53. Xu J, Cao S, Brenner T, et al. Supramolecular chemistry in molten sulfur: preorganization effects leading to marked enhancement of carbon nitride photoelectrochemistry. *Adv Funct Mater* 2015;25:6265-71. DOI
54. Wang L, Li B, You Z, et al. Heterojunction of vertically arrayed MoS_2 nanosheet/N-doped reduced graphene oxide enabling a nanozyme for sensitive biomolecule monitoring. *Anal Chem* 2021;93:11123-32. DOI
55. Li Q, Luan X, Xiao Z, et al. Ultrafast microwave synthesis of Ru-doped MoP with abundant P vacancies as the electrocatalyst for hydrogen generation in a wide pH range. *Inorg Chem* 2023;62:9687-94. DOI
56. Yuan Y, Yin L, Cao S, et al. Microwave-assisted heating synthesis: a general and rapid strategy for large-scale production of highly crystalline g-C_3N_4 with enhanced photocatalytic H_2 production. *Green Chem* 2014;16:4663-8. DOI
57. Yu Y, Zhou Q, Wang J. The ultra-rapid synthesis of 2D graphitic carbon nitride nanosheets via direct microwave heating for field emission. *Chem Commun* 2016;52:3396-9. DOI PubMed
58. Yang S, Gong Y, Zhang J, et al. Exfoliated graphitic carbon nitride nanosheets as efficient catalysts for hydrogen evolution under visible light. *Adv Mater* 2013;25:2452-6. DOI
59. Zhang X, Xie X, Wang H, Zhang J, Pan B, Xie Y. Enhanced photoresponsive ultrathin graphitic-phase C_3N_4 nanosheets for bioimaging. *J Am Chem Soc* 2013;135:18-21. DOI PubMed
60. Niu P, Zhang L, Liu G, Cheng H. Graphene-like carbon nitride nanosheets for improved photocatalytic activities. *Adv Funct Mater* 2012;22:4763-70. DOI
61. Han Q, Wang B, Gao J, et al. Atomically thin mesoporous nanomesh of graphitic C_3N_4 for high-efficiency photocatalytic hydrogen evolution. *ACS Nano* 2016;10:2745-51. DOI
62. Lakhi KS, Park DH, Al-Bahily K, et al. Correction: mesoporous carbon nitrides: synthesis, functionalization, and applications. *Chem Soc Rev* 2017;46:560. DOI
63. Yan Q, Zhao C, Zhang L, et al. Facile two-step synthesis of porous carbon nitride with enhanced photocatalytic activity using a soft template. *ACS Sustain Chem Eng* 2019;7:3866-74. DOI
64. Yang Z, Zhang Y, Schnepp Z. Soft and hard templating of graphitic carbon nitride. *J Mater Chem A* 2015;3:14081-92. DOI

65. Liu Z, Ma J, Hong M, Sun R. Potassium and sulfur dual sites on highly crystalline carbon nitride for photocatalytic biorefinery and CO_2 reduction. *ACS Catal* 2023;13:2106-17. DOI
66. Zheng D, Huang C, Wang X. Post-annealing reinforced hollow carbon nitride nanospheres for hydrogen photosynthesis. *Nanoscale* 2015;7:465-70. DOI
67. Fihri A, Bouhrara M, Patil U, Cha D, Saih Y, Polshettiwar V. Fibrous nano-silica supported ruthenium (KCC-1/Ru): a sustainable catalyst for the hydrogenolysis of alkanes with good catalytic activity and lifetime. *ACS Catal* 2012;2:1425-31. DOI
68. Li X, Zhang J, Chen X, et al. Condensed graphitic carbon nitride nanorods by nanoconfinement: promotion of crystallinity on photocatalytic conversion. *Chem Mater* 2011;23:4344-8. DOI
69. Wang Y, Wang X, Antonietti M, Zhang Y. Facile one-pot synthesis of nanoporous carbon nitride solids by using soft templates. *ChemSusChem* 2010;3:435-9. DOI
70. Yan H. Soft-templating synthesis of mesoporous graphitic carbon nitride with enhanced photocatalytic H_2 evolution under visible light. *Chem Commun* 2012;48:3430-2. DOI PubMed
71. Xin Q, Shah H, Nawaz A, et al. Antibacterial carbon-based nanomaterials. *Adv Mater* 2019;31:e1804838. DOI
72. Akhavan O, Ghaderi E. Toxicity of graphene and graphene oxide nanowalls against bacteria. *ACS Nano* 2010;4:5731-6. DOI PubMed
73. Liu S, Wei L, Hao L, et al. Sharper and faster "nano darts" kill more bacteria: a study of antibacterial activity of individually dispersed pristine single-walled carbon nanotube. *ACS Nano* 2009;3:3891-902. DOI
74. Alimohammadi F, Sharifian Gh M, Attanayake NH, et al. Antimicrobial properties of 2D MnO_2 and MoS_2 nanomaterials vertically aligned on graphene materials and Ti_3C_2 MXene. *Langmuir* 2018;34:7192-200. DOI
75. Zou X, Zhang L, Wang Z, Luo Y. Mechanisms of the antimicrobial activities of graphene materials. *J Am Chem Soc* 2016;138:2064-77. DOI PubMed
76. Zheng K, Li K, Chang T, Xie J, Chen P. Synergistic antimicrobial capability of magnetically oriented graphene oxide conjugated with gold nanoclusters. *Adv Funct Mater* 2019;29:1904603. DOI
77. Popescu A, Doyle RJ. The Gram stain after more than a century. *Biotech Histochem* 1996;71:145-51. DOI PubMed
78. Dallavalle M, Calvaresi M, Bottoni A, Melle-Franco M, Zerbetto F. Graphene can wreak havoc with cell membranes. *ACS Appl Mater Interfaces* 2015;7:4406-14. DOI PubMed
79. Cui H, Gu Z, Chen X, et al. Stimulating antibacterial activities of graphitic carbon nitride nanosheets with plasma treatment. *Nanoscale* 2019;11:18416-25. DOI
80. Sharma RK, Yadav S, Dutta S, et al. Silver nanomaterials: synthesis and (electro/photo) catalytic applications. *Chem Soc Rev* 2021;50:11293-380. DOI PubMed PMC
81. Yang B, Chen Y, Shi J. Reactive oxygen species (ROS)-based nanomedicine. *Chem Rev* 2019;119:4881-985. DOI
82. Zhao C, Tian L, Zou Z, et al. Revealing and accelerating interfacial charge carrier dynamics in Z-scheme heterojunctions for highly efficient photocatalytic oxygen evolution. *Appl Catal B Environ* 2020;268:118445. DOI
83. Chen P, Ou X, Xia C, et al. Construction of dual Z-scheme g-C_3N_4/$BiVO_4$ (040)/In_2S_3 photocatalyst for efficient photocatalytic degradation and sterilization under solar light irradiation. *Appl Surf Sci* 2024;643:158665. DOI
84. Rather RA, Lo IMC. Photoelectrochemical sewage treatment by a multifunctional g-C_3N_4/Ag/AgCl/$BiVO_4$ photoanode for the simultaneous degradation of emerging pollutants and hydrogen production, and the disinfection of *E. coli*. *Water Res* 2020;168:115166. DOI
85. Li G, Nie X, Chen J, et al. Enhanced visible-light-driven photocatalytic inactivation of Escherichia coli using g-C_3N_4/TiO_2 hybrid photocatalyst synthesized using a hydrothermal-calcination approach. *Water Res* 2015;86:17-24. DOI
86. Ni L, Zhu Y, Ma J, et al. Improved anti-biofouling performance of CdS/g-C_3N_4/rGO modified membranes based on in situ visible light photocatalysis in anammox membrane bioreactor. *J Membr Sci* 2021;620:118861. DOI
87. Yang X, Ye Y, Sun J, Li Z, Ping J, Sun X. Recent advances in g-C_3N_4-based photocatalysts for pollutant degradation and bacterial disinfection: design strategies, mechanisms, and applications. *Small* 2022;18:e2105089. DOI
88. Deng J, Liang J, Li M, Tong M. Enhanced visible-light-driven photocatalytic bacteria disinfection by g-C_3N_4-AgBr. *Colloids Surf B* 2017;152:49-57. DOI
89. Li Y, Liu X, Tan L, et al. Eradicating multidrug-resistant bacteria rapidly using a multi functional g-C_3N_4@ Bi_2S_3 nanorod heterojunction with or without antibiotics. *Adv Funct Mater* 2019;29:1900946. DOI
90. Zhang C, Li Y, Wang C, Zheng X. Different inactivation behaviors and mechanisms of representative pathogens (Escherichia coli bacteria, human adenoviruses and Bacillus subtilis spores) in g-C_3N_4-based-metal-free visible-light-enabled photocatalytic disinfection. *Sci Total Environ* 2021;755:142588. DOI PubMed PMC
91. Yan Y, Zhou X, Yu P, Li Z, Zheng T. Characteristics, mechanisms and bacteria behavior of photocatalysis with a solid Z-scheme Ag/AgBr/g-C_3N_4 nanosheet in water disinfection. *Appl Catal A Gen* 2020;590:117282. DOI
92. Gao B, Dou M, Wang J, et al. Efficient persulfate activation by carbon defects g-C_3N_4 containing electron traps for the removal of antibiotics, resistant bacteria and genes. *Chem Eng J* 2021;426:131677. DOI
93. Wang Z, Dong K, Liu Z, et al. Corrigendum to "activation of biologically relevant levels of reactive oxygen species by Au/g-C_3N_4 hybrid nanozyme for bacteria killing and wound disinfection". *Biomaterials* 2020;233:119754. DOI
94. Zhao H, Yu H, Quan X, et al. Fabrication of atomic single layer graphitic-C_3N_4 and its high performance of photocatalytic disinfection under visible light irradiation. *Appl Catal B Environ* 2014;152-3:46-50. DOI

95. Che S, Zhou X, Zhang L, Su D, Wang T, Wang C. Construction of a 2D layered phosphorus-doped graphitic carbon nitride/BiOBr heterojunction for highly efficient photocatalytic disinfection. *Chem Asian J* 2022;17:e202200095. DOI PubMed
96. Xia P, Cao S, Zhu B, et al. Designing a 0D/2D S-scheme heterojunction over polymeric carbon nitride for visible-light photocatalytic inactivation of bacteria. *Angew Chem Int Ed* 2020;59:5218-25. DOI
97. He N, Guo Z, Zhang C, et al. Bifunctional 2D/2D g-C_3N_4/BiO_{2-x} nanosheets heterojunction for bacterial disinfection mechanisms under visible and near-infrared light irradiation. *J Hazard Mater* 2022;436:129123. DOI
98. Dong M, Li Q, Xiao F, Wang Y, Yang D, Yang Y. Remarkably enhanced light and Ultrasonic-Boosting Peroxidase-like activity of g-C_3N_4-Cu-TCPP for antimicrobial applications. *Appl Surf Sci* 2023;633:157537. DOI
99. Wang Z, Dong K, Liu Z, et al. Activation of biologically relevant levels of reactive oxygen species by Au/g-C_3N_4 hybrid nanozyme for bacteria killing and wound disinfection. *Biomaterials* 2017;113:145-57. DOI
100. Wu Y, Xu W, Jiao L, et al. Defect engineering in nanozymes. *Mater Today* 2022;52:327-47. DOI
101. Wang L, Gao F, Wang A, et al. Defect-rich adhesive molybdenum disulfide/rGO vertical heterostructures with enhanced nanozyme activity for smart bacterial killing application. *Adv Mater* 2020;32:e2005423. DOI
102. Anwar A, Imran M, Iqbal HM. Smart chemistry and applied perceptions of enzyme-coupled nano-engineered assemblies to meet future biocatalytic challenges. *Coord Chem Rev* 2023;493:215329. DOI
103. Dai X, Liu H, Cai B, et al. A bioinspired atomically thin nanodot supported single-atom nanozyme for antibacterial textile coating. *Small* 2023;19:e2303901. DOI
104. Ni Y, Wang R, Zhang W, et al. Graphitic carbon nitride (g-C_3N_4)-based nanostructured materials for photodynamic inactivation: synthesis, efficacy and mechanism. *Chem Eng J* 2021;404:126528. DOI
105. Zhang P, Sun D, Cho A, et al. Modified carbon nitride nanozyme as bifunctional glucose oxidase-peroxidase for metal-free bioinspired cascade photocatalysis. *Nat Commun* 2019;10:940. DOI PubMed PMC
106. Li Y, Li Y, Ma S, et al. Efficient water disinfection with Ag_2WO_4-doped mesoporous g-C_3N_4 under visible light. *J Hazard Mater* 2017;338:33-46. DOI
107. Teng Z, Yang N, Lv H, et al. Edge-functionalized g-C_3N_4 nanosheets as a highly efficient metal-free photocatalyst for safe drinking water. *Chem* 2019;5:664-80. DOI
108. Peng L, Wang H, Li G, Zhang W, Liang Z, An T. Photocatalytic inactivation of airborne bacteria onto g-C_3N_4/TiO_2/Ni-polydopamine/Ni bifunctional coupling filter with non-size dependent capture effect. *Appl Catal B Environ* 2023;329:122580. DOI
109. Wang L, Zhang X, Yu X, et al. An All-organic semiconductor C_3N_4/PDINH heterostructure with advanced antibacterial photocatalytic therapy activity. *Adv Mater* 2019;31:e1901965. DOI
110. Peng X, Ma J, Zhou Z, et al. Molecular assembly of carbon nitride-based composite membranes for photocatalytic sterilization and wound healing. *Chem Sci* 2023;14:4319-27. DOI PubMed PMC
111. Guo J, Zhou J, Sun Z, et al. Enhanced photocatalytic and antibacterial activity of acridinium-grafted g-C_3N_4 with broad-spectrum light absorption for antimicrobial photocatalytic therapy. *Acta Biomater* 2022;146:370-84. DOI
112. Ma W, Pan J, Ren W, et al. Fabrication of antibacterial and self-cleaning CuxP@g-C_3N_4/PVDF-CTFE mixed matrix membranes with enhanced properties for efficient ultrafiltration. *J Membr Sci* 2022;659:120792. DOI
113. Chen C, Chen L, Zhu X, Chen B. Graphene nanofiltration membrane intercalated with AgNP@g-C_3N_4 for efficient water purification and photocatalytic self-cleaning performance. *Chem Eng J* 2022;441:136089. DOI
114. Xiong Q, Chen Y, Xu T, Zhu Z, Chen W, Lu W. Highly efficient purification of emerging pollutants and bacteria in natural water by g-C_3N_4-sheltered fibers containing TiO_2. *Appl Surf Sci* 2021;559:149839. DOI
115. Li R, Ren Y, Zhao P, Wang J, Liu J, Zhang Y. Graphitic carbon nitride (g-C_3N_4) nanosheets functionalized composite membrane with self-cleaning and antibacterial performance. *J Hazard Mater* 2019;365:606-14. DOI